RPG acts as a central determinant for infectosome formation and cellular polarization during intracellular rhizobial infections

Beatrice Lace[1,*], Chao Su[1], Daniel Invernot Perez[1], Marta Rodriguez-Franco[1], Tatiana Vernié[2], Morgane Batzenschlager[1], Sabrina Egli[1], Cheng-Wu Liu[3] and Thomas Ott[1,4,*]

[1] *University of Freiburg, Faculty of Biology, Cell Biology, Schänzlestr. 1, 79104 Freiburg, Germany*

[2] *LRSV, Université de Toulouse, CNRS, UPS, INP Toulouse, 31326 Castanet-Tolosan, France.*

[3] *School of Life Sciences, Division of Life Sciences and Medicine, MOE Key Laboratory for Membraneless Organelles and Cellular Dynamics, University of Science and Technology of China, Hefei 230027, China*

[4] *CIBSS – Centre of Integrative Biological Signalling Studies, University of Freiburg, Freiburg, Germany*

*Corresponding authors: beatrice.lace@biologie.uni-freiburg.de; thomas.ott@biologie.uni-freiburg.de

ABSTRACT

Host-controlled intracellular accommodation of nitrogen-fixing bacteria is essential for the establishment of a functional Root Nodule Symbiosis (RNS). In many host plants, this occurs via transcellular tubular-structures (infection threads - ITs) that extend across cell layers via polar tip-growth. Comparative phylogenomic studies have identified RPG (RHIZOBIUM-DIRECTED POLAR GROWTH) among the critical genetic determinants for bacterial infection. In *Medicago truncatula*, RPG is required for effective IT progression within root hairs but the cellular and molecular function of the encoded protein remain elusive.

26 Here, we show that RPG resides in the protein complex formed by the core endosymbiotic
27 components VAPYRIN (VPY) and LUMPY INFECTION (LIN) required for IT polar growth, co-
28 localizes with both VPY and LIN in IT tip- and perinuclear-associated puncta of *M. truncatula* root
29 hairs undergoing infection and is necessary for VPY recruitment to puncta. Fluorescence Lifetime
30 Imaging Microscopy (FLIM) of phosphoinositide species during bacterial infection revealed that
31 functional RPG is required to sustain strong membrane polarization at the advancing tip of the IT. In
32 addition, loss of RPG functionality alters the cytoskeleton-mediated connectivity between the IT tip
33 and the nucleus and affects polar secretion of the cell wall modifying enzyme NODULE PECTATE
34 LYASE (NPL). Our results integrate RPG into a core host machinery required to support symbiont
35 accommodation, suggesting that its occurrence in plant host genomes is essential to co-opt a
36 multimeric protein module committed to endosymbiosis to sustain IT-mediated bacterial infection.
37

38 **INTRODUCTION**

39 Legumes have evolved the capacity to maintain a mutualistic association with endosymbiotic
40 nitrogen-fixing rhizobia, hosting them in specialized lateral root organs, the nodules, where bacteria
41 convert atmospheric nitrogen (N_2) to ammonia (NH_4^+) and release it to the plant in exchange for
42 carbohydrates. By granting them access to an additional source of nitrogen, the Root Nodule
43 Symbiosis (RNS) allows plants to overcome nitrogen limitation occurring in terrestrial ecosystems
44 and agriculturally used sites. Thus, the transfer of this ability to cereals has been identified as one
45 possible strategy to reduce the use of environmentally harmful and expensive industrial fertilizers (S.
46 E. Bloch et al., 2020; Mus et al., 2016; Oldroyd & Dixon, 2014; Pankievicz et al., 2019; Rogers &
47 Oldroyd, 2014). Such an engineering approach however, requires an in depth understanding of the
48 molecular machineries allowing rhizobial infections of legume roots.
49 In most cases, this host-controlled process requires a molecular dialogue between the partners, which
50 involves the perception of bacterial lipo-chitooligosaccharide (LCOs) molecules called Nod factors
51 (NFs) by plasma membrane-resident receptor complexes including the *Medicago truncatula* LysM

52 receptor-like kinase NFP and its *Lotus japonicus* ortholog NFR5 (Limpens et al., 2003; Radutoiu et
53 al., 2003). Symbiont recognition triggers the onset of a signaling cascade involving the generation
54 and decoding of nuclear-associated calcium oscillations, which mediates symbiosis-related gene
55 expression (Singh et al., 2014). Interestingly, the same pathway is activated by perception of
56 diffusible signals produced by arbuscular mycorrhizal (AM) fungi, including both LCOs and long-
57 chain chitooligosaccharides (COs), although these are perceived by a different combination of
58 receptors (Feng et al., 2019; Sun et al., 2015). This common symbiosis signaling pathway shares a
59 number of genetic components including the machinery to decode the specific calcium signature
60 (Kistner et al., 2005) and few downstream factors such as VAPYRIN (VPY), a Major Sperm Domain-
61 and ankyrin-repeat-containing protein, that is required for both symbiotic interactions (Murray et al.,
62 2011; Pumplin et al., 2010). Although some structural features are shared between the AM symbiosis
63 and RNS during intracellular colonization, others are remarkably different. A whole set of those RNS-
64 specific responses is controlled by the master regulator NIN, a transcription factor orchestrating the
65 transcriptional reprogramming of cells required to sustain bacterial accommodation and concomitant
66 cell proliferation to induce the formation of a nodule primordium (Schauser et al., 1999; C. W. Liu et
67 al., 2019a; Vernié et al., 2016). This spatial and temporal coordination of infection and nodule
68 organogenesis represents a hallmark of RNS (Oldroyd & Downie, 2008).
69 Intracellular invasion of rhizobia is uniquely enabled by a membrane-confined transcellular tunnel
70 called the infection thread (IT). In many legumes such as *M. truncatula* and *L. japonicus* IT formation
71 is initiated from an infection chamber (IC) (Fournier et al., 2015) that forms upon curling of a growing
72 root hair and subsequent entrapping of rhizobia (Callaham & Torrey, 1981). Repolarization of
73 targeted secretion towards this compartment enables local cell wall modifications (e.g. by secretion
74 of the NODULE PECTATE LYASE (NPL) to the IC (Liu et al., 2019a)) leading to its radial
75 expansion (Fournier et al., 2015) and a highly confined local invagination of the plasma membrane,
76 which marks the onset of IT initiation (Gage, 2004). The IT then extends through the trichoblast and
77 subsequently progresses transcellularly through the root cortex (Libbenga & Harkes, 1973). IT

78 maintenance and progression requires a highly coordinated interplay between the migrating nucleus,
79 a cytosolic column ahead of the IT, actin and dense microtubule arrays (Fournier et al., 2015; Perrine-
80 Walker et al., 2014; Qiu et al., 2015; Timmers et al., 1999; Yokota et al., 2009). IT propagation in
81 underlying cortical tissues is supported by repolarization of these cells, forming pre-infection thread
82 (PIT) structures (Van Brussel et al., 1992). This ensures guidance of the symbionts towards the newly
83 divided cortical cells constituting the core of the nodule primordium. There, rhizobia are released
84 from the ITs into the host cell, where they differentiate into nitrogen-fixing bacteroids (Vasse et al.,
85 1990).
86 Over the last decades, reverse and forward genetics have identified several genes required for
87 bacterial infection (Roy et al., 2020; Tsyganova et al., 2021). Among these is *RHIZOBIUM-*
88 *DIRECTED POLAR GROWTH (RPG)*, which is specifically expressed upon rhizobial inoculation
89 and encodes a protein of unknown function (Arrighi et al., 2008). A loss of RPG in *M. truncatula*
90 results in the development of aberrant ITs and poorly colonized nodules (Arrighi et al., 2008). Nuclear
91 localization of RPG when heterologously over-expressed in *Nicotiana benthamiana* leaf epidermal
92 cells suggested a putative role as a transcription factor (Arrighi et al., 2008), but its cellular and
93 molecular function in *M. truncatula* have not been understood in detail. The protein, however,
94 recently re-gained great attention, when two independent comparative phylogenomic studies
95 identified *NFP*, *NIN* and *RPG* as the only genes that have been consistently lost in non-nodulating
96 species belonging to the Fagales/Fabales/Cucurbitales/Rosales (FaFaCuRo) clade (Griesmann et al.,
97 2018; van Velzen et al., 2018). This evolutionary pattern linking these genes and the ability to form
98 RNS makes them prime candidates for engineering symbiotic nitrogen fixation in cereals.
99 Here, we demonstrate that RPG is an essential component of the infectosome complex (Liu et al.,
100 2019a; Roy et al., 2020). This multi-protein assembly associates with the very tip of growing ITs and
101 with the nuclear periphery. A loss-of function mutation in *RPG* entirely blocks the recruitment of
102 VPY to the infectosome. Furthermore, a highly confined membrane polarity domain at the IT tip,
103 cytoskeleton connectivity between this site and the nucleus and targeted secretion to the IT are

104 aberrant in an *rpg* mutant. Thus, we propose that RPG provides specificity to a conserved cellular
105 machinery that enables rhizobial accommodation.
106
107 **RESULTS**
108 ***RPG* controls development of infection thread structures in *M. truncatula***
109 An ethyl methanesulfonate (EMS)-induced mutant of *M. truncatula* accession A17 (hereafter named
110 *rpg-1,* Figure 1A) was previously reported to develop enlarged ITs and poorly colonized nodules
111 (Arrighi et al., 2008), indicating that *RPG* is required for rhizobial infection. In order to genetically
112 confirm this function, we isolated a second independent, homozygous mutant allele from the *M.*
113 *truncatula Tnt1* transposon insertion collection in the R108 accession carrying an insertion at 948bp
114 downstream of the start codon (NF11990, hereafter named *rpg-2*, Figure 1A). We phenotypically
115 analyzed both mutant alleles in parallel. Confocal imaging of infected root hairs 35 days post-
116 inoculation (dpi) with a fluorescent GFP-tagged strain of the compatible symbiont *S. meliloti* (*S.*
117 *meliloti*-GFP) revealed similar alterations of IT morphology in both *rpg* mutants, with ITs showing a
118 distinctive bulbous and thick appearance compared to straight and thin ITs of their corresponding
119 wild-types (Figure 1B). To better characterize and quantitatively evaluate this peculiar IT phenotype,
120 we scored the diameter of the tube at three different points along the IT (proximal to the infection
121 chamber, intermediate and distal, Figure 1C). While the diameter size of ITs developed by the wild-
122 type had little variation (Figure 1D), reflecting the tight regulation exerted by the host over
123 development of this tubular structure, the diameter of ITs formed in roots of the *rpg* mutants was
124 highly variable and significantly wider at all measure points (Figure 1D). Altogether, this indicates
125 loss of stringent host-controlled IT maintenance in these mutants.
126 Despite their defective growth, ITs of both *rpg* mutants occasionally penetrated cortical cell layers.
127 To examine the morphology of cortical ITs with cellular resolution, we cleared and imaged roots at
128 14 dpi with *S. meliloti*-mCherry and stained them with the cell wall stain Calcofluor white to highlight
129 the cell borders. Similar to what we observed in root hairs, ITs within cortical cells appeared

130 consistently enlarged and bulbous in roots of both *rpg* mutants alleles compared to their wild-type
131 genotypes, indicating that *RPG* is required to control IT development in both epidermal and cortical
132 cell layers (Figure 1-figure supplement 1A).
133 We next compared the nodulation capacity of the mutant alleles by quantifying the number and type
134 of nodules formed 21 dpi with *S. meliloti*-LacZ. We found that nodular structures formed on roots of
135 both *rpg* mutant alleles, but the total number of infected nodules was significantly reduced compared
136 to their corresponding wild-types. In addition, *rpg* mutants failed to develop fully elongated nodules
137 at this time point (Figure 1-figure supplement 1B). This further supports the hypothesis that *RPG* is
138 not required to initiate nodule organogenesis but is essential for efficient infection and full
139 colonization. Nodulation defects were more pronounced in *rpg-2* than in *rpg-1*, which well correlates
140 with previous findings showing that a mutation within the infection-related gene *LIN,* which is
141 required for IT growth, affects more severely nodule development when occurring in the genetic
142 background R108 compared to A17 (Guan et al., 2013).
143 To assess the relevance of *RPG* for bacterial release inside nodules, we examined ultra-thin sections
144 of infected nodules formed on *rpg-1* and A17 WT via transmission electron microscopy (TEM). TEM
145 micrographs of nodule infected cells revealed larger IT structures present in nodule tissues of *rpg-1*
146 compared to WT but WT-like cell organization and symbiosome morphology (Figure 1E), indicating
147 that normal IT development in nodules requires *RPG*, but bacterial release and differentiation are not
148 directly dependent on this gene.
149 Altogether these data genetically confirm that *RPG* is essential to sustain efficient bacterial infection
150 in *M. truncatula* and clearly support a role in controlling proper assembly and progression of infection
151 thread structures in host root tissues.
152
153 **The coiled-coil domain of RPG is necessary for infection thread maintenance**
154 To further understand how RPG mediates IT maintenance, we analyzed the molecular determinants
155 required to mediate the functionality of the encoded protein during infection of root hairs.

156 *RPG* encodes a 1255 aa long protein with an N-terminal segment containing a putative nuclear
157 localization signal (NLS) and an N-terminal C2 domain (NT-C2) predicted to mediate membrane
158 tethering (Zhang et al., 2010), linked by a serine-rich intrinsically disordered region (IDR) to a long
159 alpha-helical C-terminal extension with several predicted coiled-coil (CC) regions possibly mediating
160 oligomerization (Figure 2A). A similar structural organization and high degrees of sequence
161 conservation of the NT-C2 domain and the N-terminal part of the coiled-coil region were found in
162 several homologous proteins (Arrighi et al., 2008, Figure 2-figure supplement 1). However, since any
163 of these proteins remained uncharacterized at the functional and molecular level, the contribution of
164 the structural features to protein functionality are unknown.
165 To gain more insights into the structural requirements for RPG functionality, we generated a series
166 of truncation derivatives corresponding to i) the alpha-helical C-terminal coiled-coil region (aa 331-
167 1255, RPG-CC; Figure 2A), ii) an N-terminal truncated version of the coiled-coil region, lacking the
168 region conserved among RPG homologues (aa474-1255; RPG-tCC; Figure 2A) and iii) the N-
169 terminal part containing the NLS, the NT-C2 domain and the disordered region (1-330; RPG-NT;
170 Figure 2A). To further extend localization pattern analysis, we additionally produced N-terminal
171 mCherry fusions of the full-length protein (RPG-FL; Figure 2A) and all truncated variants.
172 Functionality of the constructs was first assessed by testing their capability to genetically complement
173 IT morphology when expressed in *rpg-1* roots under the control of a functional native *RPG* promoter.
174 Mutant plants expressing mCherry-RPG-FL phenocopied the WT-like IT morphology, indicating that
175 N-terminal tagging does not impair protein functionality during IT development within root hairs
176 (Figure 2B-C). Interestingly, we found that the sole coiled-coil region of RPG (mCherry-RPG-CC)
177 was equally able to significantly restore the morphological defects of *rpg-1* ITs, even though with
178 lower efficiency when directly compared to RPG-FL (Figure 2B-C). This ability was fully dependent
179 on the N-terminal 143 aa of this region, as expression of mCherry-RPG-tCC did not rescue the *rpg-1*
180 IT phenotype (Figure 2B-C). This suggests that major molecular determinants conferring
181 functionality to RPG reside in its coiled-coil domain. This was further supported by the fact that the

182 mCherry-NT variant alone did not restore normal IT growth in the *rpg-1* mutant (Figure 2B-C). On
183 the other side, the lower complementation efficacy of mCherry-RPG-CC compared to mCherry-RPG-
184 FL (Figure 2C) clearly indicates the relevance of the N-terminal region for full RPG functionality and
185 further suggests that the NLS, the NT-C2 domain and the disordered region might constitute an
186 important regulatory unit required to fine-tune the protein function or regulate its stability.
187

188 **RPG resides in the VPY-LIN-EXO70H4 protein complex and modulates VPY recruitment to**
189 **puncta**

190 To analyze RPG localization patterns, we performed live-cell imaging of WT *M. truncatula* roots
191 (A17) expressing mCherry-RPG-FL under the control of the native *RPG* promoter. Following
192 rhizobial inoculation, the RPG protein consistently coalesced into few discrete cytoplasmic puncta
193 that were visible in both uninfected and infected root hairs imaged 4-5 dpi (Figure 3A). In uninfected
194 root hairs, such puncta were found in the vicinity of the tip (uRH; Figure 3A) while in curled root
195 hairs at the early stage of infection, these puncta located in close proximity to the infection chamber
196 (IC), often adjacent to the entrapped bacteria (IC; Figure 3A). In root hairs harboring growing ITs,
197 RPG-labelled puncta were systematically present in the perinuclear cytoplasm and associated with
198 the tip of the extending IT (IT; Figure 3A). Closer inspection showed that IT tip-associated puncta
199 encased the growing IT tip ahead of progressing bacteria (Figure 3-figure supplement 1A). When ITs
200 exhibited multiple branches, RPG-labelled puncta associated to the tip of each branch (Figure 3-
201 figure supplement 1B). Occasionally, RPG signal was observed in the nucleus and the cytoplasm of
202 infected root hairs, but its intensity was markedly weaker compared to the signal intensity detected
203 in the puncta (Figure 3-figure supplement 1C-D). These data indicate that RPG preferentially
204 accumulates in cytoplasmic puncta associated to infection sites during bacterial accommodation
205 within root hairs. This is in contrast to the exclusive nuclear localization previously reported for RPG
206 when being ectopically expressed in *N. benthamiana* leaves (Arrighi et al., 2008). While we also
207 observed nuclear localization of RPG upon constitutive, heterologous over-expression in *N.*

208 *benthamiana* leaves, we additionally detected RPG signal accumulating in the nucleolus and in
209 perinuclear-localizing structures (Figure 3-figure supplement 2). Such accumulation of RPG in
210 perinuclear structures was markedly enhanced by addition of the silencing suppressor p19 (Figure 3-
211 figure supplement 2).
212 To evaluate the contribution of RPG protein domains to its punctate localization, we analyzed the
213 subcellular patterning of the RPG deletion derivatives expressed under the control of the native *RPG*
214 promoter in roots of composite *rpg-1 M. truncatula* plants. When expressed in this mutant
215 background, mCherry-RPG-FL exhibited a comparable localization pattern to what was observed in
216 the WT background (Figure 3-figure supplement 3A). We found that both mCherry-RPG-CC and
217 mCherry-RPG-tCC accumulated to bright punctate structures as mCherry-RPG-FL, while the
218 mCherry-RPG-NT signal remained diffuse in the cytoplasm and preferentially accumulated in the
219 nucleus of transformed root hairs (Figure 3-figure supplement 3B-D). These results indicate that the
220 coiled-coil domain is necessary and sufficient for RPG localization to discrete puncta and that
221 deletion of residues from 331 to 473, although abolishing its functionality, does not affect its
222 localization to these foci (Figure 2A-C and Figure 3-figure supplement 3B-C). In addition, the
223 consistent nuclear accumulation of mCherry-RPG-NT compared to the occasional localization in this
224 compartment that we observed for RPG-FL, suggests that the coiled-coil domain determines the
225 preferential retention of the protein to cytoplasmic puncta (Figure 3-figure supplement 1C-D and
226 Figure 3-figure supplement 3D).
227 This subcellular patterning resembles the recently described localization of the so-called
228 "infectosome" complex formed by VPY, LIN and EXO70H4. These proteins systematically co-
229 localize and interact in IT tip- and perinuclear-associated cytoplasmic puncta during root hair
230 infection (Liu et al., 2019b; Roy et al., 2020). Thus, we tested if RPG is a component of this protein
231 complex. For this, we first co-expressed mCherry-RPG and VPY-GFP under the control of their
232 respective native promoters in roots of composite *M. truncatula* WT plants and imaged them at 4-5
233 dpi with *S. meliloti*-mCherry. Since the signal from co-expressed RPG- and VPY- fluorophore fusions

234 were weak, to increase its detection and to unambiguously distinguish it from background
235 fluorescence, we applied Fluorescent Lifetime Imaging Microscopy (FLIM). By performing multiple
236 cycles of excitation and detection of photon arrival times, this method increases the intensity of
237 fluorescence emission. Furthermore, it allows to analyze its decay profile, thereby enabling an
238 increased spatial resolution of genetically encoded fluorophores according to their peculiar lifetimes
239 (GFP ~ 2.5-2.7 ns; mCherry ~ 1.4-1.5 ns, Sarkisyan et al., 2015; Seefeldt et al., 2008) and the
240 subtraction of the autofluorescence signal, having similar spectral characteristics but significantly
241 shorter lifetimes (see materials and methods for more details). We found that mCherry-RPG clearly
242 co-localized with VPY-GFP in punctate structures located at the tip of the IT and in the cytoplasm
243 connecting the nucleus to the IT tip of infected root hairs (Figure 3B-C). A VPY-GFP signal of
244 weaker intensity was also diffusely visible in the cytoplasm, as previously reported (Liu et al., 2019b)
245 (Figure 3B-C). Co-expression of GFP-RPG with mCherry-LIN, the latter under the control of the
246 constitutive *Ubiquitin* promoter from *L. japonicus* (pLjUbi), also resulted in distinct co-localization
247 of the two proteins in root hairs undergoing infection (Figure 3-figure supplement 4A-B). Here, FLIM
248 enabled a clear separation of mCherry-LIN from the signal of the NLS-3xmScarlet transformation
249 marker (lifetime ~ 3.5-3.9 ns, Bindels et al., 2016, 2020) (Figure 3-figure supplement 4A-B).
250 Furthermore, we performed co-immunoprecipitation (Co-IP) assays using protoplasts obtained from
251 agroinfiltrated *N. benthamiana* leaves constitutively co-expressing RPG, VPY and EXO70H4 in
252 different combinations of pairs. Using anti-mCherry nanobody traps on protein extracts from
253 protoplasts, revealed that GFP-RPG and mCherry-RPG co-purified with mCherry-EXO70H4 and
254 VPY-GFP, respectively (Figure 3D), indicating that these proteins indeed belong to the same
255 complex.
256 Since the characteristic punctate localization of VPY is triggered by rhizobial inoculation and does
257 not depend on functional LIN (Liu et al., 2019a), we hypothesized that VPY accumulation in these
258 puncta may be triggered by and dependent on RPG, as *RPG* expression is induced in root hairs starting
259 from 2 days following inoculation with *S. meliloti* (Arrighi et al., 2008; Liu et al., 2019a). To test this,

260 we expressed VPY-GFP in roots of WT and *rpg-1* composite plants and visualized its spatial
261 patterning in root hairs at 4-7 dpi with *S. meliloti*-mCherry. Indeed, while we systematically observed
262 bright VPY-positive puncta in infected (18/19 in a total number of 8 plants) and uninfected (6/8 in a
263 total number of 6 plants) root hairs of transformed WT roots, we never detected such punctate
264 subcellular structures in *rpg-1* transformed root hairs, neither infected (19/19 events in a total number
265 of 10 plants) nor uninfected (8/8 events in a total number of 7 plants). In all cases VPY exhibited a
266 diffuse cytoplasmic signal (Figure 3E and Figure 3-figure supplement 5A). In few instances (5/19
267 infection events found in 2 plants out of 10), we observed VPY accumulating close to bacteria
268 entrapped within a curl, seemingly surrounding the site of membrane invagination occurring at the
269 early stage of IT emergence, but no cytoplasmic or perinuclear-associated puncta were visible (Figure
270 3-figure supplement 5B). This is in sharp contrast to what we observed in WT root hairs at a similar
271 stage of infection (Figure 3-figure supplement 5B).
272 From these results we conclude that RPG is a key component of the infectosome machinery
273 controlling IT polar growth, being necessary to modulate rhizobial-induced focusing of VPY to IT-
274 tip and perinuclear-associated puncta during this process. The predicted function of the infectosome
275 and the loss of VPY recruitment to IT-tip associated puncta in *rpg-1,* which fails to develop thin and
276 elongated infection threads, strongly suggest that RPG is required to sustain localized polarity at this
277 specific symbiotic domain.
278
279 **RPG is required to maintain PI(4,5)P_2 enrichment on the membrane of the IT tip.**
280 In tip-growing plant cells such as root hairs and pollen tubes, confined polarity at the apical membrane
281 domain is sustained by local enrichment of the low abundant phosphoinositide species PI(4,5)P_2,
282 which serve as landmarks to recruit diverse protein effectors regulating cytoskeleton rearrangements,
283 vesicle trafficking and signaling (Ischebeck et al., 2010; Noack & Jaillais, 2020). As the polarized IT
284 tip likely recruits part of the machinery controlling polarity establishment during root hair growth
285 (Gage, 2004), we hypothesized that local enrichment of PI(4,5)P_2 occurs at the site of symbiont

286 accommodation. To test this, we expressed the well-characterized genetically encoded PI(4,5)P_2
287 biosensor mCitrine-2xPH^{PLC} (Simon et al., 2014) under the control of the infection-induced *ENOD11*
288 promoter (Boisson-Dernier et al., 2005; Journet et al., 2001) in roots of WT *M. truncatula* composite
289 plants and analyzed its localization patterns following inoculation with *S. meliloti*-mCherry (4-8 dpi).
290 To increase the robustness of our analysis, we adopted a systematic FLIM-based approach that
291 allowed us to i) unambiguously identify local membrane enrichment of the mCitrine-PH^{PLC} probe
292 (Lifetime ~ 3 ns; Söhnel et al., 2016) and discriminate it from cell wall autofluorescence (Lifetime $\leq$
293 1.1 ns) and ii) integrate lifetime measurements obtained from the observation of multiple events in a
294 visually-intuitive form using the Phasor approach (Malacrida et al., 2021; Ranjit et al., 2018) and
295 statistically compare them (Figure 4-figure supplement 1A; see materials and methods for full
296 description).
297 In uninfected growing root hairs, PI(4,5)P_2 enriched at the apical membrane domain (Figure 4-figure
298 supplement 2A and Figure 4-figure supplement 4A) while at the onset of infection PI(4,5)P_2 was
299 locally and specifically enriched at the membrane surrounding invading bacteria emerging from the
300 infection chamber (IC) (Figure 4A – IC and Figure 4-figure supplement 4B). This indicates that
301 symbiont accommodation coincides with membrane polarization at this host-microbe interface. In
302 root hairs harboring actively growing ITs, we consistently observed local enrichment of the
303 phosphoinositide on the membrane surrounding the tip and the terminal part of the extending tube,
304 connected to the nucleus by a dense column of cytoplasm (Figure 4A – IT and Figure 4-figure
305 supplement 4C), confirming that bacterial progression is associated with strong polarization of the IT
306 membrane. Notably, we observed that local PI(4,5)P_2 enrichment also occurred on the basal
307 membrane of root hairs hosting polarized ITs extending within a cytoplasmic column connected to
308 the root hair base, and on the apical membrane of underlying cortical neighboring cells (Figure 4A –
309 CC, Figure 4-figure supplement 2B and Figure supplement 4D). This fully coincided with the
310 reorganization of the cortical cell cytoplasm into a dense central column occupied by the nucleus,
311 which is typical of pre-infection thread (PIT) responses (Van Brussel et al., 1992) (Figure 4A - CC

312 and Figure 4-figure supplement 2B). This demonstrates that local membrane polarization occurs on
313 the trajectory of IT propagation and might serve to direct local changes of the cell wall and apoplastic
314 space in preparation for the transcellular passage of the bacteria.
315 To further verify that the observed membrane localization of the 2xPH^{PLC} biosensor reflects PI(4,5)P_2
316 enrichment, we generated a mutant version of the probe bearing amino acid substitutions R37D and
317 R40D, which substantially reduce its PI(4,5)P_2-binding capacity and abolish its interaction with the
318 plasma membrane (mCitrine-2xPH$^{PLC\text{-}mut}$; Yagisawa et al., 1998; Ivanov & Harrison, 2019).
319 Expression of this mutated probe under the control of the *ENOD11* promoter in WT transgenic roots
320 resulted in exclusively diffuse cytoplasmic signal in both uninfected root hairs (Figure 4-figure
321 supplement 3 - uRH), infected root hairs (Figure 4-figure supplement 3 – IC and IT) and in cortical
322 cells underlying primary infection events (Figure 4-figure supplement 3 - CC) imaged at 4-7 dpi with
323 *S. meliloti*-mCherry.
324 Next, we evaluated the impact of a loss of RPG on infection-dependent membrane repolarization by
325 expressing the PI(4,5)P_2 probe in *rpg-1* transgenic roots and monitoring its distribution pattern upon
326 inoculation (*S. meliloti* mCherry, 4-8 dpi). Here, the apex of uninfected growing root hairs was
327 labelled by the PI(4,5)P_2 biosensor as in the WT (Figure 4-figure supplement 2A and Figure 4-figure
328 supplement 4A). PI(4,5)P_2 patterning was also similar to WT at the very initial stage of bacterial
329 accommodation, where we observed a local enrichment occurring on the membrane surrounding the
330 bacteria protruding from the IC (Figure 4A – IC and figure 4-figure supplement 4B). Thus, RPG is
331 not required to establish membrane polarization at this stage. However, PI(4,5)P_2 failed to strongly
332 enrich on the majority of membranes (21/33 IT from 10 plants) of typically enlarged infection threads
333 developed by the *rpg-1* mutant. Here, the signal of the probe remained either low and uniformly
334 labelling the membrane, cytoplasmic or almost absent (Figure 4A, Figure 4-figure supplement 2C
335 and Figure 4-figure supplement 4C), indicating that functional RPG is required to maintain IT
336 polarization during symbiont accommodation. When present, the enrichment was often found on
337 short membrane protrusions formed at multiple polar sites on the enlarged infection structures

338 developed within *rpg-1* root hairs, further supporting that not the establishment but rather the
339 maintenance and restriction of symbiont-induced polarization is RPG-dependent (Figure 4-figure
340 supplement 2C and Figure 4-figure supplement 4C). In addition, we found that development of polar
341 domains at the base of infected root hairs and on the apical membrane of underlying cortical cells
342 was not affected in *rpg-1* (Figure 4A – CC and Figure 4-figure supplement 4D), implying that RPG
343 is not necessary for these pre-infection responses but exclusively for IT maintenance and progression.
344 This is in agreement with previous findings showing that PIT formation and microtubule
345 rearrangements in cortical cells of *rpg-1* are not perturbed (Arrighi et al., 2008). However, such
346 responses were uncoupled from IT polarization and nuclear-guided progression of the tube within the
347 root hair (Figure 4A-CC), suggesting that functional RPG is important to maintain synchronization
348 between cells during the infection process.
349 To provide statistical support to our analysis, we compared the Phasor fingerprint of fluorescence
350 emission (see Materials and Methods for a detailed description) at different membrane domains
351 analyzed in multiple cells of different plants for each genotype (Figure 4-figure supplement 4E). A
352 statistical difference was only found on the Phasor position of fluorescence emission at the IT
353 membrane but not at other domains (Figure 4-figure supplement 4E).
354 To further characterize and compare the membrane identity of WT and *rpg-1* ITs, we co-visualized
355 the distribution of PI(4,5)P_2 together with its synthetic precursor PI4P, which is highly enriched at
356 the plasma membrane (PM) of plant cells and contributes to define its identity (Simon et al., 2016).
357 For this, we co-expressed mCitrine-2xPH^{PLC} with the PI4P biosensor mCherry-2xPH^{FAPP1} (Simon et
358 al., 2014) both under the control of the *ENOD11* promoter in roots of WT and *rpg-1* composite plants.
359 To avoid that the intense signal from fluorescently-labelled bacterial symbionts could interfere with
360 visualization of any of the two biosensors, we inoculated composite plants with a non-fluorescent
361 rhizobial strain (*S. meliloti*-LacZ).
362 In WT infected root hairs, we found that the tip-polarized enrichment of the PI(4,5)P_2 biosensor on
363 the IT membrane spatially coincided with low enrichment of PI4P probe, which instead preferentially

364 accumulated on the root hair PM (Figure 4B and Figure 4-figure supplement 5). Such differential
365 membrane enrichment of the two biosensors was much reduced in *rpg-1* infected root hairs, where
366 PI4P was similarly enriched on the root hair PM and on the infection thread membrane, the latter
367 being characterized by low accumulation of the PI(4,5)P_2 probe (Figure 4B and Figure 4-figure
368 supplement 5). These observations support our previous set of data, clearly indicating a role for RPG
369 in sustaining localized membrane polarization at the tip of the IT.
370 Since PI(4,5)P_2-enriched membrane domains constitute important platforms steering cytoskeleton
371 rearrangements and targeted vesicle delivery (Bloch et al., 2016; Doumane et al., 2020; Stanislas et
372 al., 2018; Synek et al., 2021) and as a last set of experiments to verify the role of RPG in maintaining
373 localized polarity at the IT tip, we decided to test how microtubule organization and polar secretion
374 associated to this symbiotic domain are affected in *rpg-1*.
375
376 **Tip-to-nucleus microtubule connectivity is perturbed in *rpg-1***
377 During IT growth, a dense array of endoplasmic microtubules (EMTs) connects the IT tip to the
378 nucleus migrating towards the root hair base and maintenance of such functional connection is
379 thought to be necessary to guide IT progression within host cells (Timmers et al., 1999; Perrine-
380 Walker et al., 2014; Fournier et al., 2008; Faehraeus, 1957).
381 Since nuclear movement appeared uncoupled from IT growth in *rpg-1* (Figure 4A - CC), we tested if
382 the tip-to-nucleus connectivity is perturbed in *rpg-1* by comparing microtubule organization in WT
383 and *rpg-1* root hairs harboring ITs using live-cell imaging. To reduce possible perturbations of
384 microtubule dynamics given by ectopic expression of exogenous tubulin isoforms (Celler et al.,
385 2016), we labelled microtubules expressing an N-terminal GFP fusion of an endogenous tubulin beta
386 isoform (*Medtr8g107250,* hereafter SYMTUB) up-regulated in infected root hairs (Breakspear et al.,
387 2014) under the control of a native 1.6kb promoter (pSYMTUB::eGFP-SYMTUB) in WT and *rpg-1*
388 roots. In most of WT root hairs hosting growing ITs imaged at 4-8dpi with *S. meliloti*-mCherry, EMTs
389 were organized in a dense cone-shape array anchored to the nucleus and extending towards the IT

390 tip, keeping a tight connection between these two poles (Figure 5A). This patterning is consistent
391 with previous reports (Timmers 1999; Perrine-Walker et al., 2014), supporting the validity of our
392 marker. When imaging *rpg-1* infected root hairs at the same time points, such connection appeared
393 loosened in the majority of cases, as EMTs associated to the IT mostly appeared dispersed and
394 stretched, no longer bridging the tip and the nucleus and often positioned at a consistent distance
395 away from the infection site (Figure 5A). Notably, the IT tip often appeared mis-oriented with respect
396 to the direction of growth, pointing towards the root hair shank instead of following the repositioning
397 of the nucleus down the root hair, suggesting that loss of nuclear-mediated IT guidance occurs in *rpg-*
398 *1*. This indicates that RPG is required to maintain a functional physical connection between the
399 nucleus and the extending tip.
400
401 **Polar secretion of NPL requires functional RPG**
402 The cell wall modifying enzyme NPL, which is essential for IT initiation and elongation in both *L.*
403 *japonicus* and *M. truncatula* (Xie et al., 2012; Liu et al., 2019a) is secreted to the IT apoplast and
404 accumulates particularly at IT tip regions in *M. truncatula* (Liu et al., 2019a), strongly suggesting that
405 its tip-targeted secretion is required for IT polar extension. To evaluate the role of RPG in NPL
406 targeting, we compared the localization pattern of this enzyme in WT and *rpg-1* infected root hairs.
407 For this, we expressed an NPL-GFP fusion under the control of the native *NPL* promoter in WT and
408 *rpg-1* roots and imaged infected root hairs at 4-8 dpi. In WT root hairs harboring growing ITs and in
409 agreement with a previous report (Liu et al., 2019a), NPL consistently showed a preferential
410 accumulation in the apoplastic space surrounding the tip when compared to the older parts of the IT
411 (Figure 5B-C). By contrast, NPL strongly accumulated in the whole lumen of the enlarged ITs
412 without any increased accumulation at a specific site in most *rpg-1* root hairs (Figure 5B-C). This
413 indicates that RPG is required to restrict the secretion domain of NPL during infection.
414

415 **DISCUSSION**

416 The capacity to intracellularly accommodate nitrogen-fixing bacteria is a hallmark of the RNS.
417 Bacterial internalization requires profound restructuring of the host cell to form an infection thread
418 compartment via polarized secretion of plasma membrane and cell wall material to a single focal
419 point. Polar progression of IT structures determines the establishment of a functional nitrogen-fixing
420 association.

421 Here, we demonstrate that RPG is a crucial component of the infectosome machinery sustaining polar
422 growth of intracellular ITs (Figure 3A-C and Figure 3-figure supplement 4 A-B), being necessary to
423 recruit VPY to the IT-tip and perinuclear puncta during IT progression within root hairs (Figure 3E
424 and Figure 3-figure supplement 5A-B). A cooperative function of RPG with the infectosome complex
425 in regulating IT polar growth is consistent with the phenotypes of *rpg*, *vpy* and *lin* mutants, exhibiting
426 strong defects in the establishment and/or the maintenance of IT progression but not being affected
427 in nodule organogenesis (Kiss et al., 2009; Murray et al., 2011; Liu et al., 2019a, Figure 1B-D and
428 Figure 1-figure supplement 1A-B). Moreover, the peculiar enlargement of ITs developed by *rpg*
429 mutants, indicative of a loss of unidirectional polarized growth, is well explained by the failure of
430 *rpg-1* to maintain the typical VPY punctate localization observed in WT root hairs (Figure 3E and
431 Figure 3-figure supplement 5A-B). Interestingly, infectosome-like and VPY-positive compartments
432 have also been observed during the arbuscular mycorrhiza symbiosis (Pumplin et al., 2010; Zhang et
433 al., 2015) and *vpy* mutants exhibit defects in this association (Feddermann et al., 2010; Pumplin et
434 al., 2010). Given the fact that VPY-recruitment into infectosome structures is abolished in an *rpg*
435 mutant, it is tempting to speculate that RPG serves as a specificity determinant for infectosome-
436 related endo- and exocytotic events during RNS, which is supported by the transcriptional
437 dependency of *RPG* from NIN (Liu et al., 2019a; Soyano & Hayashi, 2014) and is in line with *RPG*
438 being one of the few essential factors that have been lost in non-nodulating species of the FaFaCuRO
439 clade (Griesmann et al., 2018; van Velzen et al., 2018). Upon recruitment of VPY into the
440 infectosome complex it is further stabilized by LIN (Liu et al., 2019b) and this can also be assumed

441 for CERBERUS, the ortholog of LIN in *L. japonicus*, which has been shown to stabilize VPY protein
442 levels (Liu et al., 2021). Different to *RPG*, the genes encoding for VPY and LIN are retained in
443 angiosperm species forming intracellular symbioses (Radhakrishnan et al., 2020) and at least *VPY* is
444 additionally required for intracellular accommodation of the fungal partner during arbuscular
445 mycorrhizal symbiosis (Feddermann et al., 2010; Pumplin et al., 2010).
446 While the existence of infectosomes is supported by this and other studies (Liu et al., 2019b; Zhang
447 et al., 2015), the full nature of this presumably membrane-less compartment remains to be
448 investigated further. It is, however, tempting to draw parallels to the so called "polarisome", a
449 macromolecular complex regulating polarized growth of yeasts and fungal hyphae (Xie & Miao,
450 2021). Polarisomes are dense spot-like structures localized at the site of polarized growth and are
451 formed by a number of core components and many cooperative interactors (Xie & Miao, 2021). The
452 polarisome is also required to maintain the Spitzenkörper (Crampin et al., 2005), a vesicle supply
453 center located at the tip during hyphal growth, whose positioning is correlated with growth
454 directionality (Riquelme & Sánchez-León, 2014). Interestingly, a myosin protein has recently been
455 shown to mediate focal packing of the polarisome (Dünkler et al., 2021). The structural similarity of
456 the RPG C-terminal extension with myosins, as supported by structural predictions and as previously
457 suggested (Arrighi et al., 2008), and the inability of VPY to localize into distinct infectosome foci,
458 further supports the hypothesis of RPG functioning as an organizational hub protein for infectosome
459 assembly and polarity maintenance during intracellular rhizobial infections. It should, however, be
460 considered that a vesicle-associated fraction of RPG as well as of the other infectosome components
461 outside the puncta might contribute to their functionalities, although these structures cannot be
462 visualized at present due to their size and/or fluorescence intensity. A possible association of RPG
463 with vesicular compartments would be compatible with the predicted membrane-binding capacity of
464 its NT-C2 domain (D. Zhang & Aravind, 2010).
465 Rendering the infectosome complex dysfunctional in *rpg* mutants results in the loss of the highly
466 polarized membrane enrichment of $PI(4,5)P_2$ (Figure 4A-B) and most likely in mistargeted secretion

467 of key factors such as NPL required for IT progression to the growing IT tip (Liu et al., 2019a; Xie
468 et al., 2012). It is noteworthy that maintenance of the IC and secretion of NPL into this apoplastic
469 compartment is unaltered in *rpg* mutants, but is unconfined during IT development (Figure 5B-C).
470 As in many eukaryotic polarized systems, where localized exocytosis targets PI(4,5)P_2-rich
471 membrane domains, accumulation of this phosphoinositide was also shown to occur on perimicrobial
472 membranes during pathogenic infections (Qin et al., 2020) and during AM symbiosis, where
473 PI(4,5)P_2 specifically accumulated at the tips of intracellular linear hyphae (Ivanov & Harrison,
474 2019). Taken together, our data strongly support the hypothesis that IT polarity requires few specific
475 factors like RPG but predominantly relies on a highly conserved mechanism as suggested earlier
476 (Gage, 2004; Yamazaki & Hayashi, 2015). While the secretion domain in curled root hairs comprises
477 the entire IC (Fournier et al., 2015), the loss of highly restricted focal polarization results in the
478 formation of enlarged ITs (Figure 1B-D). Most of these ITs progress in an undirected manner through
479 the root hairs of *rpg* mutants, as indicated by the loss of microtubule-mediated connectivity between
480 the nucleus and the IT tip (Figure 5A). Although polarization of the basal membrane domain in the
481 respective trichoblasts and formation of PITs in the outer cortical cells are unaltered (Figure 4,
482 (Arrighi et al., 2008), effective infection of nodules is impaired (Figure 1- figure supplement 1B)
483 likely because a strictly defined time window that allows transcellular IT growth through recently
484 divided cells is missed by these slowly growing ITs in the *rpg* mutant.
485

486 **MATERIALS AND METHODS**

487 **Plant material and phenotypic analysis**

488 *M. truncatula* wild-type ecotypes R108, Jemalong A17 and two *rpg* mutant alleles were used in this
489 study. *rpg-1* is a previously described EMS mutant bearing a premature stop codon in the third exon
490 of the RPG gene (Arrighi et al., 2008). Seeds of this allele were kindly provided by Clare Gough
491 (Institut National de la Recherche Agronomique de Toulouse, Toulouse, France). *rpg-2* is a *Tnt-1*
492 insertion line (NF11990) and was obtained from the Noble Research Institute (OK, USA).

493 Seeds were scarified by soaking them in sulfuric acid (H_2SO_4) 96% for 8 minutes, then rinsed six
494 times with sterile tap water and surface sterilized with a solution of 1.2% sodium hypochlorite
495 (NaClO) and 0.1% sodium dodecyl sulfate (SDS) for 1 minute. After rinsing six times with sterile
496 tap water, seeds were transferred to 1% agar/water plates and vernalized at 4° in dark for 4-5 days.
497 Seeds were then moved to 24°C in dark for 10hrs to induce germination.
498 For phenotypical analysis of IT morphology, germinated seedlings were transferred to pots containing
499 a mixture (1:1 v/v) of quartz sand (grain size 0.1-0.5 mm, Sakret) and vermiculite (0-3 mm, Terra
500 Exotica), inoculated with *S. meliloti* (Sm2011, OD_{600}=0.001, 5 mL per pot) and grown in a controlled
501 environment chamber at 24°C with a 16/8 hours light/dark photoperiod, and 70% humidity. Pots were
502 watered twice a week with tap water and fertilized once a week with a ¼ Hoagland solution containing
503 0.1mM KNH_3. Plants were harvested at 35 dpi, the root system was excised and fixed in 4% PFA
504 (paraformaldehyde). Prior to imaging, roots were washed three times with 1 x PBS (phosphate-saline
505 buffer). Infected root hairs were imaged using a confocal microscope and measurement of the
506 infection thread diameter was performed with ImageJ/(Fiji) software (Schindelin et al., 2012).
507 Infection thread diameter has been scored on 19-31 root hairs of at least 4 individual plants.
508 For morphological examination of cortical infection threads, germinated seedlings were transferred
509 to sterile plates containing solid Fahräeus medium supplemented with 0.1 mM NH_4NO_3 and grown
510 vertically in a controlled environment chamber at 24°C with a 16/8 hours light/dark photoperiod for
511 1 week before inoculating them with *S. meliloti* (RCR2011, OD_{600}=0.01). At 14 dpi the plant root
512 system was excised, fixed in 4% PFA under vacuum for 15 min and then washed twice with 1x PBS.
513 Afterwards, roots were covered with ClearSee solution (Ursache et al., 2017) and incubated for 7-10
514 days. Prior to imaging, roots were stained with Calcofluor white for 45 minutes, washed twice with
515 ClearSee and incubated for 1hr in the last wash. Cortical infection threads were then imaged using a
516 confocal microscope.
517 For phenotypic analysis of nodulation capacity, germinated seedlings were transferred to pots
518 containing Zeolite substrate (50% fraction 1.0-2.5mm, 50% fraction 0.5-1.0-mm, Symbiom),

519 inoculated with *S. meliloti* (RCR2011 pXLGD4, GMI6526, OD_{600}=0.02, 10 ml per pot) and grown
520 in a controlled environment chamber at 22°C with a 16/8 hours light/dark photoperiod, and 70%
521 humidity. Pots were watered once a week with tap water and fertilized once a week with Fahräeus
522 medium (0.5 mM NH_4NO_3). Plants were harvested 21dpi. Two independent replica were performed.
523

524 **Hairy root transformation and rhizobial inoculation**

525 Composite *M. truncatula* plants were obtained following the previously described procedure
526 (Boisson-Dernier et al., 2001). In brief, transgenic *A. rhizogenes* (ARqua1) carrying the plasmid of
527 interest was grown in liquid LB medium (5 mL) supplemented with appropriate antibiotic for 24hrs
528 until reaching an OD_{600} of approximately 0.5-0.7. 300 µl of this culture were then spread on a plate
529 containing solid LB medium with antibiotics and incubated at 28°C in dark for 48 hrs. The root
530 meristem of germinated seedlings was removed with a scalpel and the wounded part was dragged on
531 the *A. rhizogenes* solid culture before transferring seedlings to plates containing solid Fahräeus
532 medium supplemented with 0.5 mM NH_4NO_3. Transformed seedling were grown vertically in a
533 controlled environment chamber at 22°C in dark for 3 days and for additional 4 days with a 16/8
534 hours light/dark photoperiod providing shading to the root system. Afterwards, composite plants were
535 transferred to new solid Fahräeus plates (0.5 mM NH_4NO_3) and grown for 10 days at 24°C with a
536 16/8 hours light/dark photoperiod. Transformed roots expressing the fluorescent selection marker
537 were selected using a stereo microscope, untransformed roots were excised with a scalpel and
538 composite plants transferred to either solid Fahräeus medium supplemented with 0.1 mM NH_4NO_3
539 (live-cell imaging of root hairs) or to pots (complementation assays).

540 *Sinorhizobium meliloti* (Sm2011) was grown in liquid TY medium (5 mL) supplemented with
541 appropriate antibiotics for 3 days at 28°C. 100 µl of this culture were used as inoculum for a fresh
542 culture (5mL), which was grown for 24 h at 28°C. A bacterial pellet was then obtained by
543 centrifugation at 3000 rpm for 10 minutes, washed once with liquid Fahräeus medium (0.1 mM

544 NH_4NO_3) and resuspended in the same medium to the reach a final OD_{600} = 0.01 (inoculation of
545 composite plants in plates, 200 µl per plant) or OD_{600} = 0.001 (inoculation in pots, 5 mL per plant).
546

547 **Construct design**

548 Constructs used in this study were designed and assembled using Golden Gate cloning (Binder et al.,
549 2014; Weber et al., 2011). All promoters, coding sequences and genomic sequences used were
550 synthesized by Life Technologies. When internal BsaI or BpiI sites were present, individual point
551 mutations were introduced *in silico*; in case of coding and genomic sequences, silent mutations were
552 produced. A list of all L1 and L2 constructs including module composition, fluorophore linkers and
553 tagging site is provided as supplementary file (Table S1).
554 For RPG, a sequence 1777 bp upstream of the start codon was used as promoter, as described earlier
555 (Arrighi et al., 2008). The RPG coding sequence was used for complementation assays, subcellular
556 localization studies and co-immunoprecipitation assays. RPG fragments corresponding to different
557 deletion derivatives were synthesized by Life Technologies.
558 For VPY and EXO70H4, constructs were designed as described earlier (Liu et al., 2019b). For VPY,
559 the genomic sequence and a 2926 bp promoter were used. The potato ST-LS1 intron-containing
560 version of S65TGFP used as C-terminal tag to avoid leaking expression of the fluorophore in
561 agrobacteria (Liu et al., 2019b) was synthesized by Life Technologies. For EXO70H4, the coding
562 sequence was used.
563 The previously described pLjUbi::mCherry-LIN construct (Liu et al., 2019b) was used for co-
564 localization studies.
565 For subcellular localization pattern of NPL, the coding sequence and a 2038 bp promoter were used.
566 For microtubule fluorescent labelling, the coding sequence of SYMTUB was used and a sequence
567 1555 bp upstream of the start codon as promoter.

568 For expression of the phosphoinositide biosensors, a 1106 bp promoter of *ENOD11* was used.
569 Sequences of $2xPH^{PLC}$ and $2xPH^{FAPP1}$, and of $2xPH^{PLC\ mut}$ were designed according to (Simon et al.,
570 2014) and (Yagisawa et al., 1998), respectively, and synthesized by Life Technologies.
571 The sequence data from RPG, VPY, EXO70H4, LIN, NPL, SYMTUB can be found in phytozome
572 (https://phytozome.jgi.doe.gov/) with the following gene ID: RPG (Medtr1g090807), VPY
573 (Medtr6g027840), EXO70H4 (Medtr4g062330), LIN (Medtr1g090320), NPL (Medtr3g086320),
574 SYMTUB (Medtr8g107250). The sequences of $2xPH^{PLC}$ and $2xPH^{FAPP1}$ biosensors can be
575 downloaded at http://www.ens-lyon.fr/RDP/SiCE/PIPline.html.
576
577 **Complementation assays**
578 Composite *M. truncatula* plants expressing the constructs of interest were transferred to pots
579 containing a mixture of quartz sand and vermiculite (1:1 v/v), inoculated with *S. meliloti* (Sm2011,
580 OD_{600}=0.001, 5 mL per pot) and grown in a controlled environment chamber at 24°C with a 16/8
581 hours light/dark photoperiod, and 70% humidity. Pots were watered twice a week with tap water and
582 fertilized once a week with a ¼ Hoagland solution containing 0.1mM KNH_3. Plants were harvested
583 at 21dpi. Transformed roots exhibiting strong expression of the fluorescent marker were selected,
584 excised and fixed in 4% PFA (paraformaldehyde) under vacuum for 15 min. After washing the roots
585 twice with 1x PBS (phosphate-saline buffer), roots were covered with ClearSee solution (Ursache et
586 al., 2017) and incubated for 7-10 days. ClearSee solution was refreshed every two days. Prior to
587 imaging, roots were stained with Calcofluor white for 45 minutes, washed twice with ClearSee and
588 incubated for 1h in the last wash. Infected root hairs were imaged using a confocal microscope and
589 measurement of the infection thread diameter was performed with ImageJ/(Fiji) software (Schindelin
590 et al., 2012). Infection thread diameter has been scored on 20-32 independently transformed roots
591 from at least 5 plants.
592
593

594 **Live-cell imaging of root hairs**

595 Composite plants growing on solid Fahräeus medium supplemented with 0.1 mM NH_4NO_3 were
596 inoculated with *S. meliloti* (Sm2011) by adding 200 µl of bacterial suspension (OD_{600} = 0.01) on each
597 root system. Prior to inoculation, the position of the apex of transformed roots was marked on plates.
598 4-8 dpi, root segments that had grown below the mark were excised, mounted in water and root hairs
599 were imaged with a confocal microscope. For live-cell imaging experiments, at least two independent
600 replica were conducted with six composite plants (arising from independent transformation events)
601 analyzed per condition, unless otherwise stated.

602

603 **Confocal Laser-Scanning Microscopy (CLSM) and Fluorescence Lifetime Imaging Microscopy**
604 **(FLIM)**

605 All imaging was performed using a Leica SP8 FALCON confocal microscope equipped with a 20x
606 or 40x water immersion lens (Leica Microsystems, Mannheim, Germany). A White Light Laser
607 (WLL) was used as excitation source. GFP and mCitrine were excited at 488nm and the emission
608 collected at 500-550nm. mCherry and mScarlet were excited at 581nm and emission detected at 590-
609 640nm. To excite calcofluor white, a 405nm laser diode was used and emission was detected at 425-
610 475nm.

611 For Fluorescence Lifetime Imaging Microscopy, a Leica GaAsP-hybrid detector was used to collect
612 fluorescent emission. Different channels were acquired in sequential scanning between frames. A
613 pulse repetition rate of 80mHz was used with the exception that images in Figure 3B and Figure 3 –
614 figure supplement 1A were acquired using a 40mHz pulse repetition rate for the GFP/NowGFP
615 channel and the mCherry/mScarlet channel, respectively. Fluorescence emission was acquired from
616 single focal planes using 20 scan repetitions for each channel.

617

618 **Intensity-based and FLIM-based image analysis**

619 Intensity-based images were analyzed using ImageJ/(Fiji) software (Schindelin et al., 2012).

620 FLIM-based images were analyzed using LAS X SP8 Control Software (Leica Microsystems GmbH).
621 Global fitting of the intensity decay profile using n-exponential reconvolution was performed to
622 separate major fluorescent components within each channel and calculate their lifetime. The number
623 of components (n) used for curve fitting was determined according to evaluation of the chi-squared
624 ($\chi 2$) value (Lakowicz, 2006) and a threshold of 30 photons was applied to generate the final images.
625 Components with lifetime value < 1.2 ns representing autofluorescent species accumulating in plant
626 cell walls (Donaldson, 2020; Heskes et al., 2012) were subtracted from each channel.
627 All data on reconvolution of decay profiles of images presented in the article are provided as source
628 files.
629 Since global fitting does not always allow to resolve and characterize the decay profile of pixels
630 constituting minor populations within an image (Ranjit et al., 2018), the decay profile of fluorescent
631 emission of regions of interest (ROIs) selected on membrane domains was additionally analyzed for
632 the analysis and quantification of PI(4,5)P_2 membrane enrichment. n-exponential fitting of the decay
633 curve was carried out to resolve lifetime values associated to each ROI (Figure 4- figure supplement
634 1). Reconvolution data from all images and selected ROIs analyzed are provided as source files.
635 Further, the raw decay profile of each ROI was analyzed using the Phasor approach to obtain a Phasor
636 fingerprint whose position describes the fluorescent emission at that region and reflects its
637 composition in terms of relative abundance of fluorescent species (Figure 4- figure supplement 1)
638 (see Ranjit et al., 2018 and Malacrida et al., 2021 for detailed description of Phasor approach). Phasor
639 plots were generated using a second harmonic, a threshold of 22 photons and a median of 15. To
640 visualize and compare the Phasor fingerprint of ROIs selected in multiple images from different
641 genotypes, the center of mass of Phasor images depicting the pixel populations originating from each
642 ROI was calculated images using ImageJ/(Fiji) (Schindelin et al., 2012) and the obtained XM and
643 YM coordinates were plotted on a graph (Figure 4- figure supplement 1). A Mann-Whitney non-
644 parametric test was performed to detect statistically significant differences of XM and YM values.
645

646 **Statistical analysis**

647 All statistical analysis and generation of graphs were performed using GraphPad Prism software
648 (GraphPad Software Inc.). Data were subjected to a normality test to determine the statistical method
649 to apply. Kruskal-Wallis followed by Dunn's post-hoc test or Mann-Whitney were applied as non-
650 parametric tests. Raw data and results of the statistical analysis are provided as source files linked to
651 the corresponding figure.

652

653 **Transformation of *N. benthamiana* leaves, protoplast isolation and coimmunoprecipitation**
654 **assay**

655 Transgenic *Agrobacterium rhizogenes* (ARqua1) carrying the plasmid of interest were grown in
656 liquid LB media supplemented with appropriate antibiotics for 24 hours at 28°C. Bacterial cultures
657 were pelleted by centrifugation (4000 rpm), resuspended in Agromix (10 mM $MgCl_2$; 10 mM
658 MES/KOH pH 5.6; 150 uM Acetosyringone) and mixed in selected combinations to reach a final
659 OD_{600} of 0.3. An *Agrobacterium tumefaciens* (GV3101) carrying a plasmid for expression of the
660 silencing suppressor p19 was added to each mix (final OD_{600} = 0.1), which was then incubated at
661 room temperature (RT) in the dark for 2 h. The second and third leaf of 4-5 weeks old *N. benthamiana*
662 plants were infiltrated on the abaxial side using a 1 mL syringe. 72 h post-infiltration leaves were
663 harvested and protoplasts were isolated as previously described (Su et al., 2022). Isolated protoplasts
664 were directly lysed in 1 mL protein extraction buffer (50 mM Tris-HCl (pH 7.5), 150 mM NaCl, 10%
665 (v/v) glycerol, 2 mM EDTA, 5 mM DTT, 1 mM phenylmethylsulfonyl fluoride (PMSF), Protease
666 Inhibitor Cocktail (Roche), and 1% (v/v) IGEPAL CA-630 (I3021, Sigma-Aldrich)) and incubated
667 for 1 h at 4°C. Lysates were centrifuged at 13000 rpm for 30 min (at 4°C) to obtain the supernatant
668 fractions, which were then immunoprecipitated using RFP-Traps Magnetica agarose (rta, Chromotek)
669 at 4°C for 90 min. After incubation with RFP-Traps, samples were washed 5 times with washing
670 buffer (50 mM Tris-HCl (pH 7.5)), 150 mM NaCl, 10% (v/v) glycerol, 2 mM EDTA, Protease
671 Inhibitor Cocktail (cOmplete™, Mini, EDTA-free, 04693159001, Roche), and 0.5% (v/v) IGEPAL

672 CA-630 (I3021, Sigma-Aldrich)). To release the proteins, 40 µL of washing buffer and 10 µL 5x
673 protein loading buffer were added, and samples were heated for 10 min at 95°C. 10 µL of each sample
674 were then loaded on a 12% (w/v) SDS gel, run for ~90 mins (100 V, RT) and transferred overnight
675 at 30 V (at 4°C) to a polyvinylidene difluoride (PVDF) membrane (Immobilon-P, pore size 0.45 µm,
676 IPVH00010, Carl Roth). Transferred membranes were blocked with 5% (w/v) milk for 30 mins at
677 RT before being hybridized with the corresponding anti-GFP (632381, Takara) or anti-mCherry
678 (632543, Takara) antibodies at dilutions of 1:3000 and 1:2000, respectively, for 2 h at RT. Before
679 incubating with the secondary antibody (anti-mouse, A-4415; anti-rabbit, A-6514; Sigma-Aldrich) (1
680 h, RT), membranes were washed 3 times for 10 min with TBST buffer. Membranes were developed
681 following 3 washes of 10 min each with TBST buffer.

682 **Transmission electron microscopy**

683 Wild-type (A17) and *rpg-1* germinated seedlings were transferred to an aeroponic system (25 liters
684 volume), inoculated with *S. meliloti* (Sm2011, OD_{600}=0.01, 5 l) and grown in liquid Fahräeus (0.1
685 mM NH_4NO_3) that was replaced weekly. Plants were harvested 35 dpi. Nodules were cut in half and
686 immediately vacuum infiltrated for 15 min in MTSB buffer containing 4% PFA and 2.5%
687 glutaraldehyde at room temperature. Samples were left in fixative for 3 h at room temperature and
688 transferred to 4°C for overnight. Samples were washed with MTSB five times (10 min each) and post
689 fixed in a water solution of 1% OsO_4 on ice during 2.5 h. Samples were then washed with water twice
690 for 10 min followed by *in bloc* staining with 1% UrAc in water for 1.5 h. After washing the samples
691 twice with water for 5 min, they were subjected to dehydration by incubating them for 15 min each
692 in increasing EtOH/water graded series (30%. 50%, 70%, 80%, 95%) and for 30 min twice in 100%
693 EtOH and 100% Acetone. Samples were gradually embedded in Epoxi resin using resin:acetone
694 mixtures (1:3, 1:1, 3:1) 8 h each, and finally pure resin (3 times exchange, 8 h each). Embedded
695 nodules were polymerized for two days at 60°C and 70 nm sections were obtained with a Reichert-
696 Jung Ultracut-E microtome. Sections were collected on copper grids and contrasted with 2% uranyl

acetate and Reynolds lead citrate solution (Reynolds, 1963). Transmission electron microscopy images were obtained using a Philips CM10 (80 kV) microscope coupled to a GATAN Bioscan Camera Model 792.

MATERIALS AVAILABILITY STATEMENT

All materials can be requested from the corresponding authors any time.

ACKNOWLEDGEMENTS

We would like to thank Carla Brillada, Marco Trujillo and Franck A. Ditengou as well as Eija Schulze and Rosula Hinnenberg and Pascal Krohn for their experimental support and technical help, respectively, and the entire Ott lab team for the continuous inputs into the project. We would also like to thank Pierre-Marc Delaux and Jean Keller (LRSV, Université de Toulouse) for critically reading the manuscript and providing a comprehensive phylogeny on RPG, respectively, as well as Leonel Malacrida (Advanced Bioimaging Unit, IP Montevideo, Universidad de la República) for the fruitful discussions on Phasor analysis. We also thank the staff of the Life Imaging Center (LIC) in the Hilde Mangold House (HMH) of the Albert-Ludwigs-University of Freiburg for the help with their confocal microscopy resources, and the excellent support in image recording. The microscopes are operated by the Microscopy and Image Analysis Platform (MIAP) and the Life Imaging Center (LIC), Freiburg. TV belongs to the LRSV, which is part of the TULIP LABEX (ANR-10-LABX-41). The *Medicago truncatula* plants utilized in this research project, which are jointly owned by the Centre National De La Recherche Scientifique, were obtained from Noble Research Institute, LLC and were created through research funded, in part, by a grant from the National Science Foundation, NSF-0703285.

FUNDING

Engineering Nitrogen Symbiosis for Africa (ENSA) project currently supported through a grant to the University of Cambridge by the Bill & Melinda Gates Foundation (OPP1172165) and UK government's Department for International Development (DFID) (TO)

Deutsche Forschungsgemeinschaft (DFG, German Research Foundation) 431626755 (TO)

DFG under Germany's Excellence Strategy grant CIBSS – EXC-2189 – Project ID 39093984 (TO)

China Scholarship Council (CSC) grants 201708080016 (CS)

DFG project number 414136422 (CLSM; TO), DFG project number 426849454 (TEM; TO)

AUTHOR CONTRIBUTIONS

Conceptualization: BL, TO; Investigation: BL, CS, DIP, MR-F, TV, MB, SE, C-WL; Writing – Original Draft: BL, TO; Writing –Review & Editing: BL, CS, DIP, MR-F, TV, MB, SE, C-WL, TO; Supervision: BL, TO; Project administration: TO; Funding Acquisition: TO

REFERENCES

Arrighi, J. F., Godfroy, O., De Billy, F., Saurat, O., Jauneau, A., & Gough, C. (2008). The RPG gene of Medicago truncatula controls Rhizobium-directed polar growth during infection. *Proceedings of the National Academy of Sciences of the United States of America*, *105*(28), 9817–9822. https://doi.org/10.1073/pnas.0710273105

Bindels, D. S., Haarbosch, L., Van Weeren, L., Postma, M., Wiese, K. E., Mastop, M., Aumonier, S., Gotthard, G., Royant, A., Hink, M. A., & Gadella, T. W. J. (2016). MScarlet: A bright monomeric red fluorescent protein for cellular imaging. *Nature Methods*, *14*(1), 53–56. https://doi.org/10.1038/nmeth.4074

Bindels, D. S., Postma, M., Haarbosch, L., van Weeren, L., & Gadella, T. W. J. (2020). Multiparameter screening method for developing optimized red-fluorescent proteins. *Nature Protocols*, *15*(2), 450–478. https://doi.org/10.1038/s41596-019-0250-7

Binder, A., Lambert, J., Morbitzer, R., Popp, C., Ott, T., Lahaye, T., & Parniske, M. (2014). A Modular Plasmid Assembly Kit for Multigene Expression, Gene Silencing and Silencing Rescue in Plants. *PLOS ONE*, *9*(2), e88218. https://doi.org/10.1371/JOURNAL.PONE.0088218

Bloch, D., Pleskot, R., Pejchar, P., Potocký, M., Trpkošová, P., Cwiklik, L., Vukašinović, N., Sternberg, H., Yalovsky, S., & Žárský, V. (2016). Exocyst SEC3 and phosphoinositides define sites of exocytosis in pollen tube initiation and growth. *Plant Physiology*, *172*(2), 980–1002. https://doi.org/10.1104/pp.16.00690

Bloch, S. E., Ryu, M. H., Ozaydin, B., & Broglie, R. (2020). Harnessing atmospheric nitrogen for cereal crop production. *Current Opinion in Biotechnology*, *62*, 181–188. https://doi.org/10.1016/J.COPBIO.2019.09.024

Boisson-Dernier, A., Andriankaja, A., Chabaud, M., Niebel, A., Journet, E.-P., Barker, D. G., & De Carvalho-Niebel, F. (2005). MtENOD11 Gene Activation During Rhizobial Infection and Mycorrhizal Arbuscule Development Requires a Common AT-Rich-Containing Regulatory Sequence. *Molecular Plant-Microbe Interactions*, *18*(12), 1269–1276. https://doi.org/10.1094/MPMI

Boisson-Dernier, A., Chabaud, M., Garcia, F., Bécard, G., Rosenberg, C., & Barker, D. G. (2001). Agrobacterium rhizogenes-transformed roots of Medicago truncatula for the study of nitrogen-fixing and endomycorrhizal symbiotic associations. *Molecular Plant-Microbe Interactions : MPMI*, *14*(6), 695–700. https://doi.org/10.1094/MPMI.2001.14.6.695

Callaham, D. A., & Torrey, J. G. (1981). The structural basis for infection of root hairs of Trifolium repens by Rhizobium . *Canadian Journal of Botany*, *59*(9), 1647–1664. https://doi.org/10.1139/b81-223

Celler, K., Fujita, M., Kawamura, E., Ambrose, C., Herburger, K., Holzinger, A., & Wasteneys, G. O. (2016). Microtubules in Plant Cells: Strategies and Methods forImmunofluorescence,

773 Transmission Electron Microscopy and Live CellImaging. *Methods in Molecular Biology*
774 *(Clifton, N.J.)*, *1365*, 155. https://doi.org/10.1007/978-1-4939-3124-8_8

775 Crampin, H., Finley, K., Gerami-Nejad, M., Court, H., Gale, C., Berman, J., & Sudbery, P. (2005).
776 Candida albicans hyphae have a Spitzenkörper that is distinct from the polarisome found in
777 yeast and pseudohyphae. *Journal of Cell Science*, *118*(13), 2935–2947.
778 https://doi.org/10.1242/jcs.02414

779 Donaldson, L. (2020). Autofluorescence in plants. *Molecules*, *25*(10).
780 https://doi.org/10.3390/molecules25102393

781 Doumane, M., Lebecq, A., Colin, L., Fangain, A., Stevens, F. D., Bareille, J., Hamant, O.,
782 Belkhadir, Y., Munnik, T., Jaillais, Y., & Caillaud, M.-C. (2021). Inducible depletion of
783 PI(4,5)P_2 by the synthetic iDePP system in Arabidopsis. *Nature Plants*, 7, 587-597.
784 https://doi.org/10.1038/s41477-021-00907-z

785 Dünkler, A., Leda, M., Kromer, J.-M., Neller, J., Gronemeyer, T., Goryachev, A. B., & Johnsson,
786 N. (2021). Type V myosin focuses the polarisome and shapes the tip of yeast cells. *Journal of*
787 *Cell Biology*, 220(5), e202006193. https://doi.org/10.1083/jcb.202006193

788 Feddermann, N., Duvvuru Muni, R. R., Zeier, T., Stuurman, J., Ercolin, F., Schorderet, M., &
789 Reinhardt, D. (2010). The PAM1 gene of petunia, required for intracellular accommodation
790 and morphogenesis of arbuscular mycorrhizal fungi, encodes a homologue of VAPYRIN.
791 *Plant Journal*, *64*(3), 470–481. https://doi.org/10.1111/j.1365-313X.2010.04341.x

792 Feng, F., Sun, J., Radhakrishnan, G. V., Lee, T., Bozsóki, Z., Fort, S., Gavrin, A., Gysel, K.,
793 Thygesen, M. B., Andersen, K. R., Radutoiu, S., Stougaard, J., & Oldroyd, G. E. D. (2019). A
794 combination of chitooligosaccharide and lipochitooligosaccharide recognition promotes
795 arbuscular mycorrhizal associations in Medicago truncatula. *Nature Communications*, *10*(1).
796 https://doi.org/10.1038/s41467-019-12999-5

797 Fournier, J., Teillet, A., Chabaud, M., Ivanov, S., Genre, A., Limpens, E., Carvalho-Niebel, F. De,

& Barker, D. G. (2015). Remodeling of the infection chamber before infection thread formation reveals a two-step mechanism for rhizobial entry into the host legume root hair. *Plant Physiology*, *167*(4), 1233–1242. https://doi.org/10.1104/pp.114.253302

Fournier, J., Timmers, A. C. J., Sieberer, B. J., Jauneau, A., Chabaud, M., & Barker, D. G. (2008). Mechanism of infection thread elongation in root hairs of Medicago truncatula and dynamic interplay with associated rhizobial colonization. *Plant Physiology*, *148*(4), 1985–1995. https://doi.org/10.1104/pp.108.125674

Gage, D. J. (2004). Infection and Invasion of Roots by Symbiotic, Nitrogen-Fixing Rhizobia during Nodulation of Temperate Legumes. *Microbiology and Molecular Biology Reviews*, *68*(2), 280–300. https://doi.org/10.1128/mmbr.68.2.280-300.2004

Fahraeus, G. (1957). The Infection of Clover Root Hairs by Nodule Bacteria Studied by a Simple Glass Slide Technique. *Journal gen. Microbiology,* 16(2). https://doi.org/10.1099/00221287-16-2-374

Griesmann, M., Chang, Y., Liu, X., Song, Y., Haberer, G., Crook, M. B., Billault-Penneteau, B., Lauressergues, D., Keller, J., Imanishi, L., Roswanjaya, Y. P., Kohlen, W., Pujic, P., Battenberg, K., Alloisio, N., Liang, Y., Hilhorst, H., Salgado, M. G., Hocher, V., … Cheng, S. (2018). Phylogenomics reveals multiple losses of nitrogen-fixing root nodule symbiosis. *Science*, *361*(6398), 1–18. https://doi.org/10.1126/science.aat1743

Guan, D., Stacey, N., Liu, C., Wen, J., Mysore, K. S., Torres-Jerez, I., Vernié, T., Tadege, M., Zhou, C., Wang, Z. Y., Udvardi, M. K., Oldroyd, G. E. D., & Murray, J. D. (2013). Rhizobial Infection Is Associated with the Development of Peripheral Vasculature in Nodules of Medicago truncatula. *Plant Physiology*, *162*(1), 107–115. https://doi.org/10.1104/PP.113.215111

Heskes, A. M., Lincoln, C. N., Goodger, J. Q. D., Woodrow, I. E., & Smith, T. A. (2012). Multiphoton fluorescence lifetime imaging shows spatial segregation of secondary metabolites

in Eucalyptus secretory cavities. *Journal of Microscopy*, *247*(1), 33–42. https://doi.org/10.1111/j.1365-2818.2011.03593.x

Ischebeck, T., Seiler, S., & Heilmann, I. (2010). At the poles across kingdoms: Phosphoinositides and polar tip growth. *Protoplasma*, *240*(1), 13–31. https://doi.org/10.1007/s00709-009-0093-0

Ivanov, S., & Harrison, M. J. (2019). Accumulation of phosphoinositides in distinct regions of the periarbuscular membrane. *New Phytologist*, *221*(4), 2213–2227. https://doi.org/10.1111/nph.15553

Journet, E.-P., El-Gachtouli, N., Vernoud, V., De Billy, F., Pichon, M., Dedieu, A., Arnould, C., Morandi, D., Barker, D. G., & Gianinazzi-Pearson, V. (2001). Medicago truncatula ENOD11: A Novel RPRP-Encoding Early Nodulin Gene Expressed During Mycorrhization in Arbuscule-Containing Cells. *Molecular Plant-Microbe Interactions*, *14*(6), 737-748. https://doi.org/10.1094/MPMI.2001.14.6.737

Kistner, C., Winzer, T., Pitzschke, A., Mulder, L., Sato, S., Kaneko, T., Tabata, S., Sandal, N., Stougaard, J., Webb, K. J., Szczyglowski, K., & Parniske, M. (2005). Seven Lotus japonicus genes required for transcriptional reprogramming of the root during fungal and bacterial symbiosis. *Plant Cell*, *17*(8), 2217–2229. https://doi.org/10.1105/tpc.105.032714

Laetitia, M., Simon, A., Platre, M. P., Marquès-Bueno, M. M., Armengot, L., Stanislas, T., Bayle, V., Caillaud, M.-C., & Jaillais, Y. (2016). A PtdIns(4)P-driven electrostatic field controls cell membrane identity and signalling in plants. *Nature Plants*, *2*, e16089. https://doi.org/10.1038/NPLANTS.2016.89

Lakowicz, J. R. (2006). Principles of fluorescence spectroscopy. *Principles of Fluorescence Spectroscopy*, 1–954. https://doi.org/10.1007/978-0-387-46312-4

Schauser, L., Roussis, A., Stiller, J., & Stougaard, J. (1999). A plant regulator controlling development of symbiotic root nodules. *Nature*, *402*, 191-195. https://doi.org/10.1038/46058

Libbenga, K. R., & Harkes, P. A. A. (1973). Initial proliferation of cortical cells in the formation of root nodules in Pisum sativum L. *Planta,* 114(1), 17-28. https://doi.org/10.1007/BF00390281

Limpens, E., Franken, C., Smit, P., Willemse, J., Bisseling, T., & Geurts, R. (2003). LysM Domain Receptor Kinases Regulating Rhizobial Nod Factor-Induced Infection. *Science*, *302*(5645), 630–633. https://doi.org/10.1126/science.1090074

Liu, C. W., Breakspear, A., Guan, D., Cerri, M. R., Jackson, K., Jiang, S., Robson, F., Radhakrishnan, G. V., Roy, S., Bone, C., Stacey, N., Rogers, C., Trick, M., Niebel, A., Oldroyd, G. E. D., De Carvalho-Niebel, F., & Murray, J. D. (2019a). NIN Acts as a Network Hub Controlling a Growth Module Required for Rhizobial Infection. *Plant Physiology*, *179*(4), 1704–1722. https://doi.org/10.1104/PP.18.01572

Liu, C. W., Breakspear, A., Stacey, N., Findlay, K., Nakashima, J., Ramakrishnan, K., Liu, M., Xie, F., Endre, G., de Carvalho-Niebel, F., Oldroyd, G. E. D., Udvardi, M. K., Fournier, J., & Murray, J. D. (2019b). A protein complex required for polar growth of rhizobial infection threads. *Nature Communications*, *10*(1), 1–17. https://doi.org/10.1038/s41467-019-10029-y

Liu, M., Jia, N., Li, X., Liu, R., Xie, Q., Murray, J. D., Downie, J. A., & Xie, F. (2021). CERBERUS is critical for stabilization of VAPYRIN during rhizobial infection in Lotus japonicus. *New Phytologist*, *229*(3), 1684–1700. https://doi.org/10.1111/NPH.16973

Malacrida, L., Ranjit, S., Jameson, D. M., & Gratton, E. (2021). The Phasor Plot: A Universal Circle to Advance Fluorescence Lifetime Analysis and Interpretation. *Annual Review of Biophysics*, *50*, 575–593. https://doi.org/10.1146/annurev-biophys-062920-063631

Murray, J. D., Reddy, R., Muni, D., Torres-Jerez, I., Tang, Y., Allen, S., Andriankaja, M., Li, G., Laxmi, A., Cheng, X., Wen, J., Vaughan, D., Schultze, M., Sun, J., Charpentier, M., Oldroyd, G., Tadege, M., Ratet, P., Mysore, K. S., … Udvardi, M. K. (2011). Vapyrin, a gene essential for intracellular progression of arbuscular mycorrhizal symbiosis, is also essential for infection by rhizobia in the nodule symbiosis of Medicago truncatula. *The Plant Journal*, *65*(2), 244-

252. https://doi.org/10.1111/j.1365-313X.2010.04415.x

Mus, F., Crook, M. B., Garcia, K., Garcia Costas, A., Geddes, B. A., Kouri, E. D., Paramasivan, P., Ryu, M.-H., Oldroyd, G. E. D., Poole, P. S., Udvardi, M. K., Voigt, C. A., Ané, J.-M., & Peters, J. W. (2016). Symbiotic Nitrogen Fixation and the Challenges to Its Extension to Nonlegumes. *Applied and Environmental Microbiology*, *82*. https://doi.org/10.1128/AEM.01055-16

Noack, L. C., & Jaillais, Y. (2020). Functions of Anionic Lipids in Plants. *Annual Review of Plant Biology*, *71*, 71–102. https://doi.org/10.1146/annurev-arplant-081519-035910

Oldroyd, G. E. D., & Dixon, R. (2014). Biotechnological solutions to the nitrogen problem. *Current Opinion in Biotechnology*, *26*, 19–24. https://doi.org/10.1016/j.copbio.2013.08.006

Oldroyd, G. E. D., & Downie, J. A. (2008). Coordinating nodule morphogenesis with rhizobial infection in legumes. *Annual Review of Plant Biology*, *59*, 519–546. https://doi.org/10.1146/annurev.arplant.59.032607.092839

Pankievicz, V. C. S., Irving, T. B., Maia, L. G. S., & Ané, J. M. (2019). Are we there yet? The long walk towards the development of efficient symbiotic associations between nitrogen-fixing bacteria and non-leguminous crops. *BMC Biology*, *17*(1). https://doi.org/10.1186/s12915-019-0710-0

Perrine-Walker, F. M., Lartaud, M., Kouchi, H., & Ridge, R. W. (2014). Microtubule array formation during root hair infection thread initiation and elongation in the Mesorhizobium-Lotus symbiosis. *Protoplasma*, *251*(5), 1099–1111. https://doi.org/10.1007/s00709-014-0618-z

Pumplin, N., Mondo, S. J., Topp, S., Starker, C. G., Gantt, J. S., & Harrison, M. J. (2010). Medicago truncatula Vapyrin is a novel protein required for arbuscular mycorrhizal symbiosis. *The Plant Journal*, *61*(3), 482-494. https://doi.org/10.1111/j.1365-313X.2009.04072.x

896 Qin, L., Zhou, Z., Li, Q., Zhai, C., Liu, L., Quilichini, T. D., Gao, P., Kessler, S. A., Jaillais, Y.,
897 Datla, R., Peng, G., Xiang, D., & Wei, Y. (2020). Specific recruitment of phosphoinositide
898 species to the plant-pathogen interfacial membrane underlies Arabidopsis susceptibility to
899 fungal infection. *Plant Cell*, *32*(5), 1665–1688. https://doi.org/10.1105/tpc.19.00970

900 Qiu, L., Lin, J., Xu, J., Sato, S., Parniske, M., Wang, T. L., Allan Downie, J., Xie, F., & J-s, L.
901 (2015). SCARN a Novel Class of SCAR Protein That Is Required for Root-Hair Infection
902 during Legume Nodulation. *PLoS Genet*, *11*(10), 1005623.
903 https://doi.org/10.1371/journal.pgen.1005623

904 Radhakrishnan, G. V., Keller, J., Rich, M. K., Vernié, T., Mbadinga Mbadinga, D. L., Vigneron, N.,
905 Cottret, L., Clemente, H. S., Libourel, C., Cheema, J., Linde, A. M., Eklund, D. M., Cheng, S.,
906 Wong, G. K. S., Lagercrantz, U., Li, F. W., Oldroyd, G. E. D., & Delaux, P. M. (2020). An
907 ancestral signalling pathway is conserved in intracellular symbioses-forming plant lineages.
908 *Nature Plants*, *6*(3), 280–289. https://doi.org/10.1038/s41477-020-0613-7

909 Radutoiu, S., Madsen, L. H., Madsen, E. B., Felle, H. H., Umehara, Y., Grønlund, M., Sato, S.,
910 Nakamura, Y., Tabata, S., Sandal, N., & Stougaard, J. (2003). Plant recognition of symbiotic
911 bacteria requires two LysM receptor-like kinases. *Nature*, *425*(6958), 585–592.
912 https://doi.org/10.1038/nature02039

913 Ranjit, S., Malacrida, L., Jameson, D. M., & Gratton, E. (2018). Fit-free analysis of fluorescence
914 lifetime imaging data using the phasor approach. *Nature Protocols*, *13*(9), 1979–2004.
915 https://doi.org/10.1038/s41596-018-0026-5

916 Reynolds, E. S. (1963). The use of lead citrate at high pH as an electron-opaque stain in electron
917 microscopy. *The Journal of Cell Biology*, *17*, 208–212. https://doi.org/10.1083/jcb.17.1.208

918 Riquelme, M., & Sánchez-León, E. (2014). The Spitzenkörper: A choreographer of fungal growth
919 and morphogenesis. *Current Opinion in Microbiology*, *20*, 27–33.
920 https://doi.org/10.1016/j.mib.2014.04.003

921 Rogers, C., & Oldroyd, G. E. D. (2014). Synthetic biology approaches to engineering the nitrogen
922 symbiosis in cereals. *Journal of Experimental Botany*, *65*(8), 1939–1946.
923 https://doi.org/10.1093/JXB/ERU098

924 Roy, S., Liu, W., Nandety, R. S., Crook, A., Mysore, K. S., Pislariu, C. I., Frugoli, J., Dickstein, R.,
925 & Udvardi, M. K. (2020). Celebrating 20 Years of Genetic Discoveries in Legume Nodulation
926 and Symbiotic Nitrogen Fixation. *The Plant Cell*, *32*(1), 15–41.
927 https://doi.org/10.1105/tpc.19.00279

928 Sarkisyan, K. S., Goryashchenko, A. S., Lidsky, P. V., Gorbachev, D. A., Bozhanova, N. G.,
929 Gorokhovatsky, A. Y., Pereverzeva, A. R., Ryumina, A. P., Zherdeva, V. V., Savitsky, A. P.,
930 Solntsev, K. M., Bommarius, A. S., Sharonov, G. V., Lindquist, J. R., Drobizhev, M., Hughes,
931 T. E., Rebane, A., Lukyanov, K. A., & Mishin, A. S. (2015). Green Fluorescent Protein with
932 Anionic Tryptophan-Based Chromophore and Long Fluorescence Lifetime. *Biophysical*
933 *Journal*, *109*(2), 380–389. https://doi.org/10.1016/j.bpj.2015.06.018

934 Schindelin, J., Arganda-Carreras, I., Frise, E., Kaynig, V., Longair, M., Pietzsch, T., Preibisch, S.,
935 Rueden, C., Saalfeld, S., Schmid, B., Tinevez, J. Y., White, D. J., Hartenstein, V., Eliceiri, K.,
936 Tomancak, P., & Cardona, A. (2012). Fiji: An open-source platform for biological-image
937 analysis. *Nature Methods*, *9*(7), 676–682. https://doi.org/10.1038/nmeth.2019

938 Seefeldt, B., Kasper, R., Seidel, T., Tinnefeld, P., Dietz, K. J., Heilemann, M., & Sauer, M. (2008).
939 Fluorescent proteins for single-molecule fluorescence applications. *Journal of Biophotonics*,
940 *1*(1), 74–82. https://doi.org/10.1002/jbio.200710024

941 Simon, M. L. A., Platre, M. P., Assil, S., Van Wijk, R., Chen, W. Y., Chory, J., Dreux, M., Munnik,
942 T., & Jaillais, Y. (2014). A multi-colour/multi-affinity marker set to visualize phosphoinositide
943 dynamics in Arabidopsis. *Plant Journal*, *77*(2), 322–337. https://doi.org/10.1111/tpj.12358

944 Singh, S., Katzer, K., Lambert, J., Cerri, M., & Parniske, M. (2014). CYCLOPS, A DNA-binding
945 transcriptional activator, orchestrates symbiotic root nodule development. *Cell Host and*

946 *Microbe*, *15*(2), 139–152. https://doi.org/10.1016/J.CHOM.2014.01.011

947 Söhnel, A. C., Kohl, W., Gregor, I., Enderlein, J., Rieger, B., & Busch, K. B. (2016). Probing of
948 protein localization and shuttling in mitochondrial microcompartments by FLIM with sub-
949 diffraction resolution. *Biochimica et Biophysica Acta - Bioenergetics*, *1857*(8), 1290–1299.
950 https://doi.org/10.1016/J.BBABIO.2016.03.021

951 Soyano, T., & Hayashi, M. (2014). Transcriptional networks leading to symbiotic nodule
952 organogenesis. *Current Opinion in Plant Biology*, *20*, 146–154.
953 https://doi.org/10.1016/J.PBI.2014.07.010

954 Stanislas, T., Platre, M. P., Liu, M., Rambaud-Lavigne, L. E. S., Jaillais, Y., & Hamant, O. (2018).
955 A phosphoinositide map at the shoot apical meristem in Arabidopsis thaliana. *BMC Biology*,
956 *16*(1). https://doi.org/10.1186/s12915-018-0490-y

957 Su, C., Rodriguez-Franco, M., Lace, B., Nebel, N., Hernandez-Reyes, C., Liang, P., Schulze, E.,
958 Popp, C., Keller, J., Libourel, C., Fischer, A. A. M., Gabor, K. E., Mymrikov, E. V., Gross, N.
959 M., Mark, E., Hunte, C., Weber, W., Wendler, P., Stanislas, T., … Ott, T. (2022). Remorin
960 proteins serves as membrane topology scaffolds in plants. *BioRxiv*, 484384.
961 https://doi.org/10.1101/2022.03.15.484384

962 Sun, J., Miller, J. B., Granqvist, E., Wiley-Kalil, A., Gobbato, E., Maillet, F., Cottaz, S., Samain, E.,
963 Venkateshwaran, M., Fort, S., Morris, R. J., Ané, J. M., Dénarié, J., & Oldroyd, G. E. D.
964 (2015). Activation of symbiosis signaling by arbuscular mycorrhizal fungi in legumes and
965 riceopen. *Plant Cell*, *27*(3), 823–838. https://doi.org/10.1105/tpc.114.131326

966 Synek, L., Pleskot, R., Sekereš, J., Serrano, N., Vukašinović, N., Ortmannová, J., Klejchová, M.,
967 Pejchar, P., Batystová, K., Gutkowska, M., Janková-Drdová, E., Marković, V., Pečenková, T.,
968 Šantřuček, J., Žárský, V., & Potocký, M. (2021). Plasma membrane phospholipid signature
969 recruits the plant exocyst complex via the EXO70A1 subunit. *Proceedings of the National*
970 *Academy of Sciences of the United States of America*, *118*(36).

https://doi.org/10.1073/pnas.2105287118

Timmers, A. C. J., Auriac, M. C., & Truchet, G. (1999). Refined analysis of early symbiotic steps of the Rhizobium-Medicago interaction in relationship with microtubular cytoskeleton rearrangements. *Development*, *126*(16), 3617–3628. https://doi.org/10.1242/dev.126.16.3617

Tsyganova, A. V., Brewin, N. J., & Tsyganov, V. E. (2021). Structure and development of the legume-rhizobial symbiotic interface in infection threads. *Cells*, *10*(5). https://doi.org/10.3390/cells10051050

Ursache, R., Grube Andersen, T., Marhav, P., & Geldner, N. (2017). A protocol for combining fluorescent proteins with histological stains for diverse cell wall components. *The Plant Journal*, *93*(2), 399-412. https://doi.org/10.1111/tpj.13784

Van Brussel, A. A. N., Bakhuizen, R., Van Spronsen, P. C., Spaink, H. P., Tak, T., Lugtenberg, B. J. J., & Kijne, J. W. (1992). Induction of pre-infection thread structures in the leguminous host plant by mitogenic lipo-oligosaccharides of rhizobium. *Science*, *257*(5066), 70–72. https://doi.org/10.1126/science.257.5066.70

van Velzen, R., Holmer, R., Bu, F., Rutten, L., van Zeijl, A., Liu, W., Santuari, L., Cao, Q., Sharma, T., Shen, D., Roswanjaya, Y., Wardhani, T. A. K., Kalhor, M. S., Jansen, J., Johan, van den H., Güngör, B., Hartog, M., Hontelez, J., Verver, J., … Geurts, R. (2018). Comparative genomics of the nonlegume Parasponia reveals insights into evolution of nitrogen-fixing rhizobium symbioses. *Proceedings of the National Academy of Sciences of the United States of America*, *115*(20), E4700–E4709. https://doi.org/10.1073/pnas.1721395115

Vasse, J., De Billy, F., Camut, S., & Truchet, G. (1990). Correlation between ultrastructural differentiation of bacteriods and nitrogen fixation in alfalfa nodules. *Journal of Bacteriology*, *172*(8), 4295–4306. https://doi.org/10.1128/jb.172.8.4295-4306.1990

Vernié, T., Kim, J., Frances, L., Ding, Y., Sun, J., Guan, D., Niebel, A., Gifford, M. L., de Carvalho-Niebel, F., & Oldroyd, G. E. D. (2016). The NIN Transcription Factor Coordinates

996 Diverse Nodulation Programs in Different Tissues of the Medicago truncatula Root. *The Plant*
997 *Cell*, *27*(12), 3410–3424. https://doi.org/10.1105/TPC.15.00461

998 Weber, E., Engler, C., Gruetzner, R., Werner, S., & Marillonnet, S. (2011). A Modular Cloning
999 System for Standardized Assembly of Multigene Constructs. *PLOS ONE*, *6*(2), e16765.
1000 https://doi.org/10.1371/JOURNAL.PONE.0016765

1001 Xie, F., Murray, J. D., Kim, J., Heckmann, A. B., Edwards, A., Oldroyd, G. E. D., & Downie, J. A.
1002 (2012). Legume pectate lyase required for root infection by rhizobia. *Proceedings of the*
1003 *National Academy of Sciences of the United States of America*, *109*(2), 633–638.
1004 https://doi.org/10.1073/pnas.1113992109

1005 Xie, Y., & Miao, Y. (2021). Polarisome assembly mediates actin remodeling during polarized yeast
1006 and fungal growth. *Journal of Cell Science*, *134*(1), 1–11. https://doi.org/10.1242/jcs.247916

1007 Yagisawa, H., Sakuma, K., Paterson, H. F., Cheung, R., Allen, V., Hirata, H., Watanabe, Y., Hirata,
1008 M., Williams, R. L., & Katan, M. (1998). Replacements of single basic amino acids in the
1009 pleckstrin homology domain of phospholipase C-δ1 alter the ligand binding, phospholipase
1010 activity, and interaction with the plasma membrane. *Journal of Biological Chemistry*, *273*(1),
1011 417–424. https://doi.org/10.1074/jbc.273.1.417

1012 Yamazaki, A., & Hayashi, M. (2015). Building the interaction interfaces: Host responses upon
1013 infection with microorganisms. *Current Opinion in Plant Biology*, *23*, 132–139.
1014 https://doi.org/10.1016/J.PBI.2014.12.003

1015 Yokota, K., Fukai, E., Madsen, L. H., Jurkiewicz, A., Rueda, P., Radutoiu, S., Held, M., Hossain,
1016 M. S., Szczyglowski, K., Morieri, G., Oldroyd, G. E. D., Downie, J. A., Nielsen, M. W.,
1017 Rusek, A. M., Sato, S., Tabata, S., James, E. K., Oyaizu, H., Sandal, N., & Stougaard, J.
1018 (2009). Rearrangement of actin cytoskeleton mediates invasion of lotus japonicus roots by
1019 Mesorhizobium loti. *Plant Cell*, *21*(1), 267–284. https://doi.org/10.1105/TPC.108.063693

1020 Zhang, D., & Aravind, L. (2010). Identification of novel families and classification of the C2

1021 domain superfamily elucidate the origin and evolution of membrane targeting activities in
1022 eukaryotes. *Gene*, *469*(1–2), 18–30. https://doi.org/10.1016/J.GENE.2010.08.006

1023 Zhang, X., Pumplin, N., Ivanov, S., & Harrison, M. J. (2015). EXO70I is required for development
1024 of a sub-domain of the periarbuscular membrane during arbuscular mycorrhizal symbiosis.
1025 *Current Biology*, *25*(16), 2189–2195. https://doi.org/10.1016/j.cub.2015.06.075

FIGURES

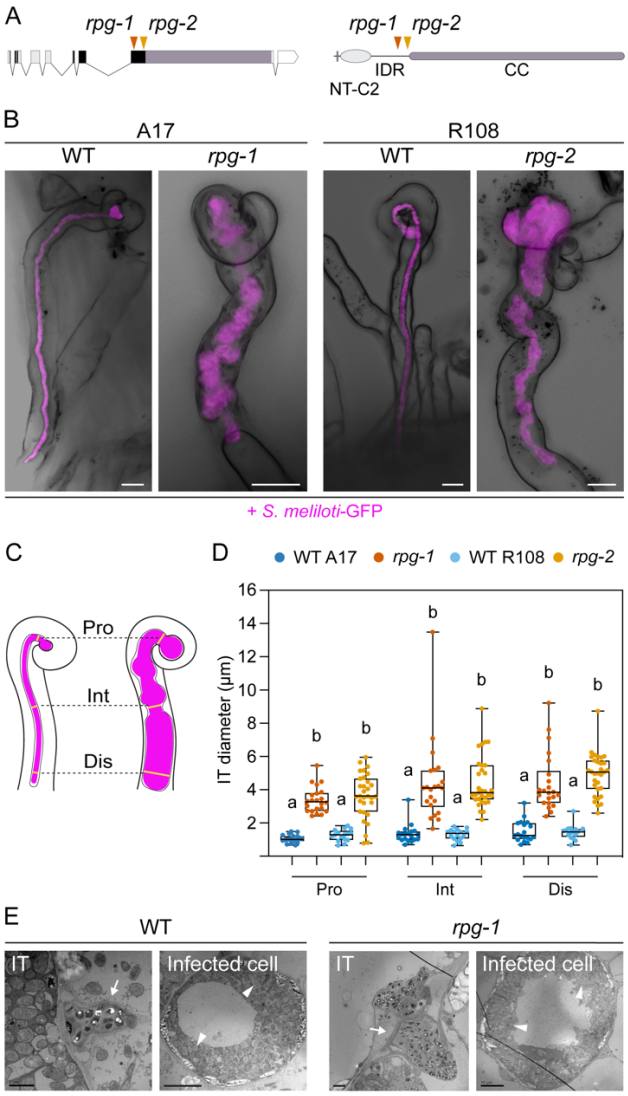

Figure 1. *RPG* is required for the maintenance of infection thread morphology. (A) Gene (left) and protein (right) structure of RPG showing the position of the mutations of two different mutant alleles (*rpg-1*, Arrighi *et al*., 2008, orange arrowhead; *rpg-2*, this study, yellow arrowhead). Both mutations map in the third exon of the *RPG* gene corresponding to the disordered region of the protein located upstream of the coiled-coil domain. NT-C2 = N-terminal C2 domain; IDR = intrinsically disordered region; CC = coiled-coil domain. **(B)** Representative confocal images of aberrant ITs formed 35 dpi within root hairs of *rpg-1* and *rpg-2* roots compared to thin and elongated ITs of the corresponding wild-types (WT). Images are overlaid of intensity projections of fluorescence and brightfield channels. *S. meliloti*-GFP is shown in magenta. Scale bars = 10 µm. **(C)** Schematic visualization of the method used to quantify morphological IT defects. The IT diameter was measured on the fluorescent channel at three different points along the IT length: in proximity of the infection chamber (Pro), in the intermediate part of the IT (Int) and in the distal part of the IT (Dis). **(D)** IT diameters scored on roots of *rpg* mutants and corresponding wild-types at the three measured points shown in **C**. In the box plot, the top and bottom of each box represents the 75th and 25th percentiles, the middle horizontal bar indicates the median and whiskers represent the range of minimum and maximum values. Letters indicate statistically significant differences according to Kruskal-Wallis multiple comparison analysis followed by Dunn's post-hoc test. The number of plants analyzed per genotype is 4 (WT A17), 5 (*rpg-1*); 4 (WT R108); 4 (*rpg-2*) with at least 2 ITs per plant being analyzed. **(E)** TEM sections obtained from WT and *rpg-1* nodules showing IT structures (arrows) with thicker appearance in *rpg-1* compared to WT. The organization of infected cells and symbiosome (arrowheads) morphology are similar in the two genotypes. Scale bars (from left to right) = 2 µm, 10 µm, 2 µm, 10 µm.

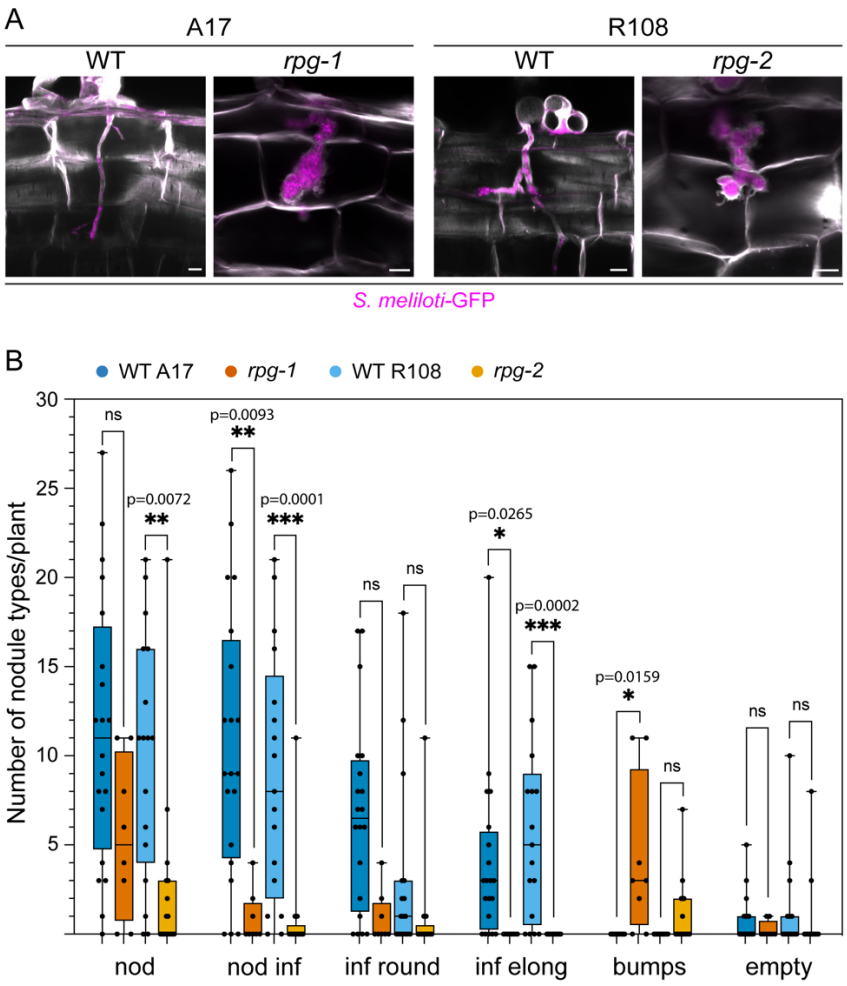

Figure 1 – figure supplement 1. Cortical infection threads and nodule phenotype of *rpg* mutants. (**A**) Confocal images of cortical ITs formed in roots of *rpg* mutants compared to their corresponding wild-types (WT) at 14 dpi with *S. meliloti-GFP* (magenta). Cell walls were stained with Calcofluor white (white). Images are a merge of intensity projections of the fluorescent channels. Scale bars = 10 µm. (**B**) Number and type of nodules formed on *rpg* mutant alleles compared to their corresponding wild-types at 21 dpi with *S. meliloti*-LacZ. Data are presented as box plots where the top and bottom of each box represents the 75th and 25th percentiles, the middle horizontal bar indicates the median and whiskers represent the range of minimum and maximum values. Asterisks indicate statistical significance based on a Kruskal-Wallis multiple comparison analysis followed by Dunn's post-hoc test with *p*-values <0.05 (*), <0.01 (**), < 0.001 (***). ns = not significant. The number of plants analyzed per genotype is 20 (WT A17), 8 (*rpg-1*), 17 (WT R108), 17 (*rpg-2*). Nod = total nodule structures; nod inf = total infected nodules; inf round = infected round nodules; inf elong = infected elongated nodules; bumps = bump-like nodules with arrested infection on the top; empty = empty nodules.

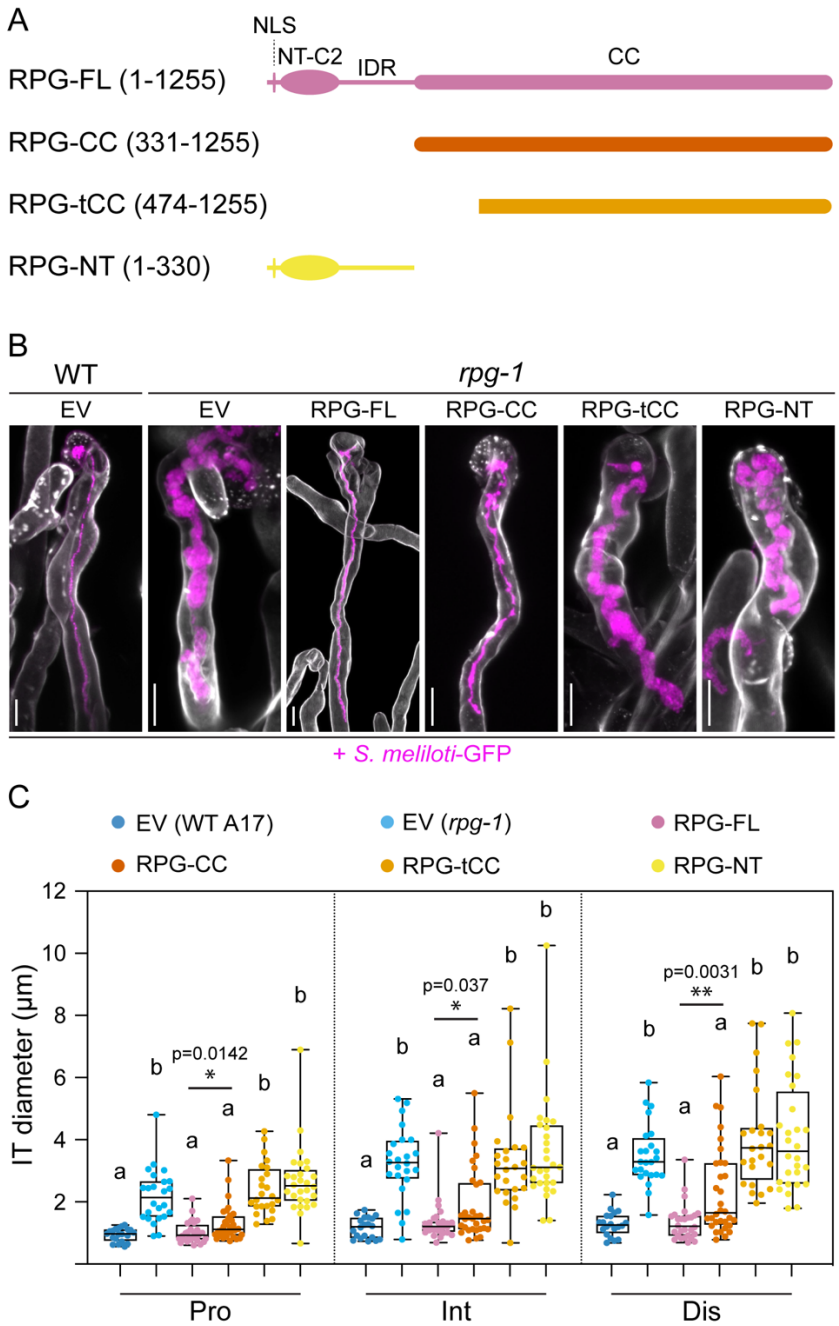

Figure 2. The coiled-coil domain of RPG is necessary to restore WT-like infection thread morphology in *rpg-1* root hairs. (A) Schematic representation of the RPG full-length protein and deletion derivatives used for complementation assays. Numbers indicate amino acids included in each fragment. NLS = nuclear localization signal; NT-C2 = N-terminal C2 domain; IDR = intrinsically disordered region; CC = coiled-coil domain. **(B)** Representative confocal images of ITs developed within root hairs of WT and *rpg-1* transgenic roots expressing the different constructs 21 dpi with *S. meliloti*-GFP (magenta). Cell walls were stained with Calcofluor white (white). Images are merge of intensity projections of fluorescent channels. EV = empty vector. Scale bars = 10 µm **(C)** IT diameters scored at the three different points schematically represented in Figure 1C. Data are presented as box plots where the top and bottom of each box represents the 75th and 25th percentiles, the middle horizontal bar indicate the median and whiskers represent the range of minimum and maximum values. Letters indicate statistically significant differences according to Kruskal-Wallis multiple comparison analysis followed by Dunn's post-hoc test. A Mann-Whitney test was performed to compare RPG-FL and RPG-CC with *p*-values <0.05 (*), <0.01 (**), < 0.001 (***). The number of composite plants analyzed per each condition is 5 (EV in WT), 6 (EV in *rpg-1*), 7 (RPG-FL), 8 (RPG-CC), 6 (RPG-tCC), 7 (RPG-NT). For each plant, 4 ITs have been analyzed.

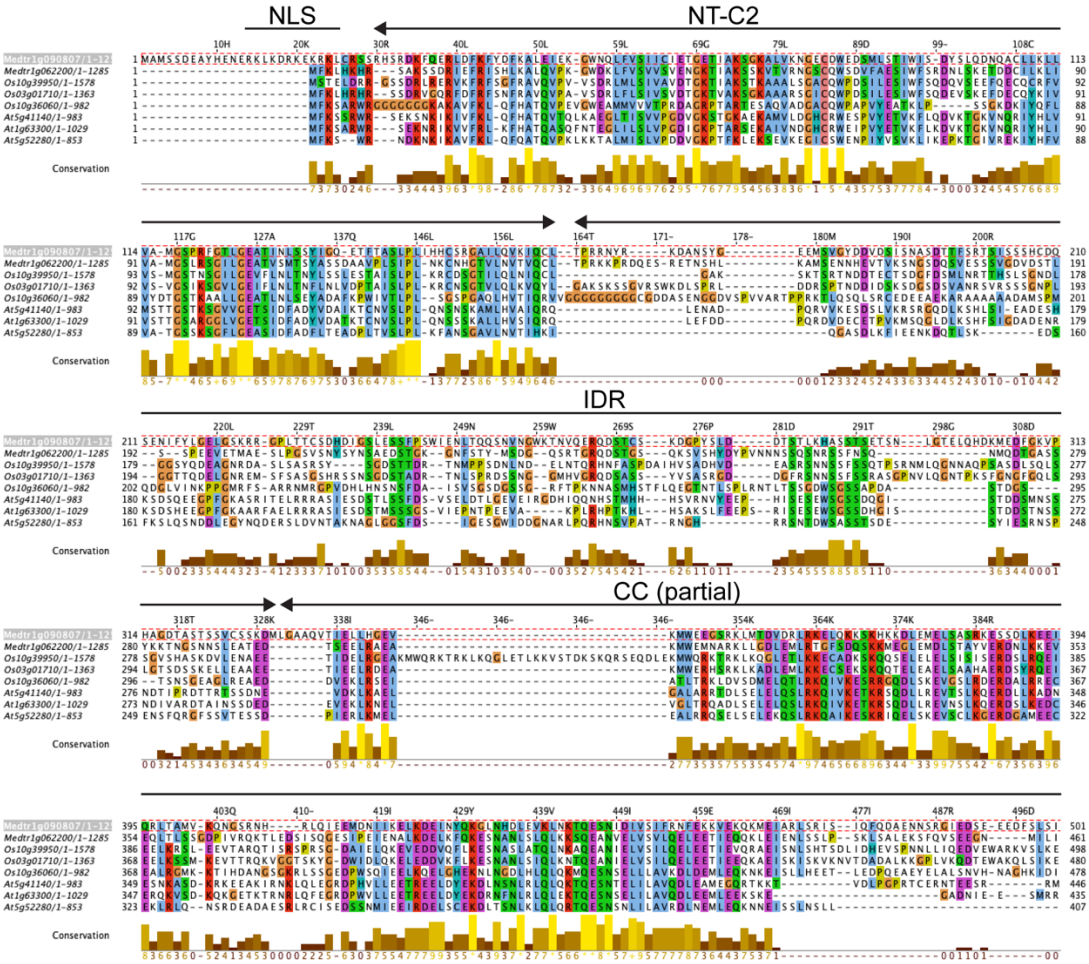

Figure 2 – figure supplement 1. Sequence conservation among RPG homologs. Amino acid conservation between the NT-C2 domains and N-terminal parts of the coiled-coil region of RPG and homologous proteins from rice (Os) and Arabidopsis (At). Sequence alignment was performed using MUSCLE and visualized with Jalview to calculate conservation scores (Procter, 2021). Amino acids are colored according to Clustal X Colour Scheme. The sequence of *M. truncatula* RPG was used as reference for numbering of residues. NLS = nuclear localization signal; NT-C2 = N-terminal C2 domain; IDR = intrinsically disordered region; CC (partial) = coiled-coil region, partial.

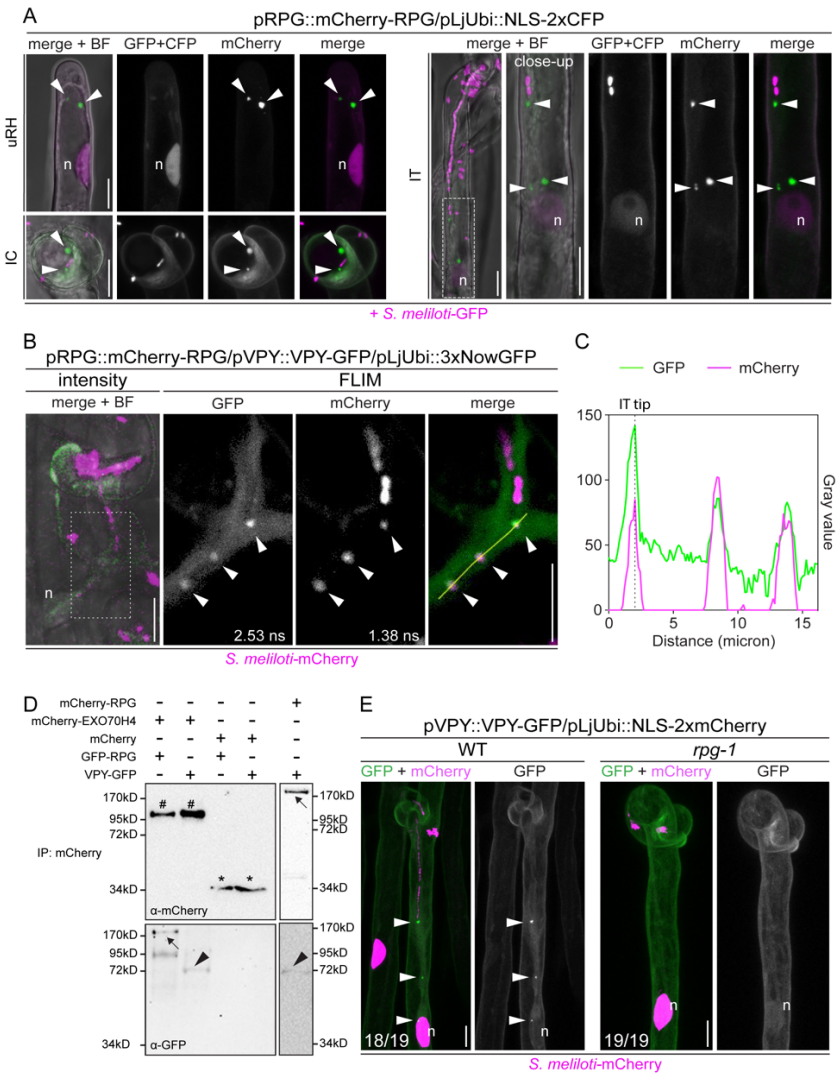

Figure 3. RPG is a key component of the VPY-LIN-EXO70H4 infectosome complex. (A) Live-cell confocal images showing mCherry-RPG localization in root hairs of WT transgenic roots at 4-5 dpi with *S. meliloti*-GFP. mCherry-RPG accumulates in cytoplasmic punctate structures (arrowheads) which are found close to the apex of uninfected root hairs (uRH), in the vicinity of rhizobia entrapped within the infection chamber of curled root hairs (IC) and associated to the perinuclear cytoplasm and the tip of infection threads (IT). The dashed white line box indicates the region shown in the close-up. A nuclear-localized tandem CFP was used as transformation marker. Images are intensity projections. Individual channels are false colored in grey. When channels are merged, the GFP/CFP channel is shown in magenta and the mCherry channel is shown in green. The bright field (BF) is overlaid with merged fluorescent channels. **(B)** Co-localization of mCherry-RPG with VPY-GFP in cytoplasmic and IT tip-associated puncta (arrowheads) in root hairs of WT transgenic roots imaged at 4-5 dpi with *S. meliloti*-mCherry. The intensity-based image is a merge of maximum intensity projections of GFP (green) and mCherry (magenta) channels overlaid with the brightfield (BF) channel. The dashed white line box indicates the region shown in FLIM images. FLIM images are maximum intensity projections of two focal planes. Lifetime values (ns) obtained from exponential reconvolution of decay profiles of GFP and mCherry channels are reported. Individual channels are shown in grey. When components are merged, GFP is shown in green and mCherry in magenta. A nuclear-localized triple NowGFP was used as transformation marker (not visible in these images). **(C)** Intensity profile of GFP and mCherry signal along the yellow transect shown in **(B)**. The intensity peaks at the infection thread tip (IT tip) are marked by a dashed black line **(D)** Co-immunoprecipitation analysis using anti-RFP nanotraps showing interaction between GFP-RPG and mCherry-EXO70H4 and between mCherry-RPG and VPY-GFP. Total proteins were extracted from protoplasts obtained from *N. benthamiana* leaves co-expressing RPG, VPY and EXO70H4 in different combination of pairs. Black arrows indicate mCherry-RPG (upper right panel) and GFP-RPG (lower left panel), hashtags indicate mCherry-EXO70H4, arrowheads indicate VPY, asterisks indicate mCherry. **(E)** Localization pattern of VPY-GFP in root hairs of WT and *rpg-1* transgenic roots imaged at 4-7 dpi with *S. meliloti*-mCherry. VPY-positive puncta (arrowheads) are systematically present in WT but not in *rpg-1* infected root hairs. Numbers indicate frequencies of observations, made on a total number of 8 (WT) and 10 (*rpg-1*) composite plants. A nuclear-localized tandem mCherry was used as transformation marker. GFP channel is shown in grey when isolated, in green when merged with mCherry (magenta). n = nucleus. Scale bars = 10 µm.

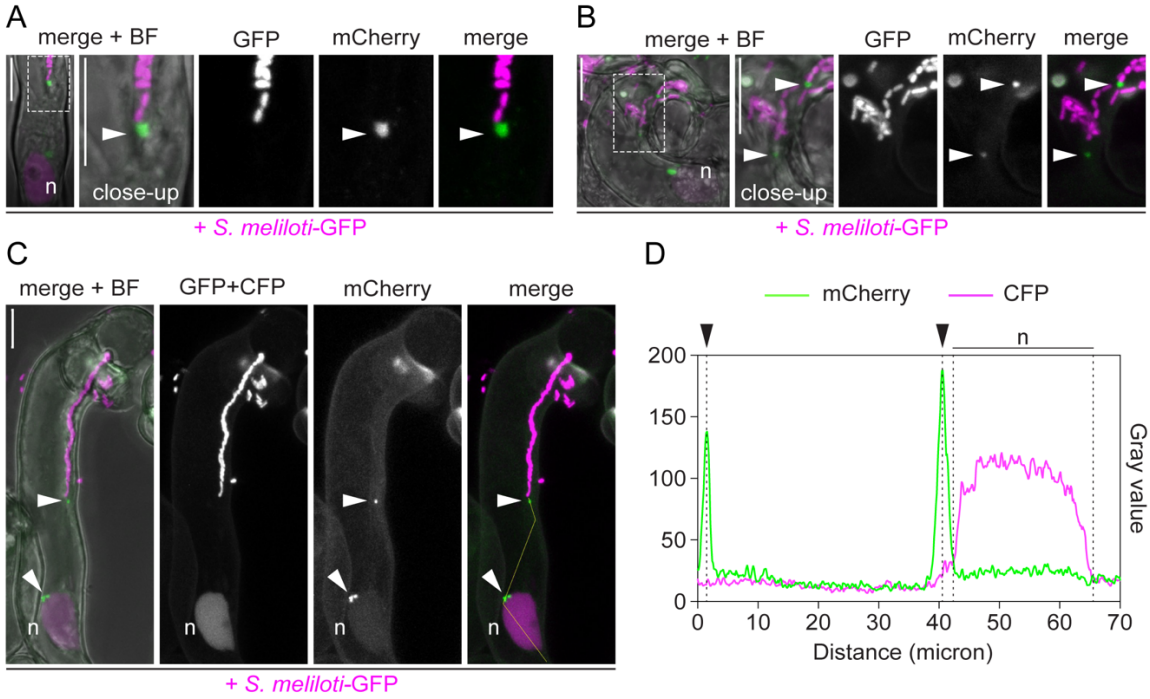

Figure 3-figure supplement 1. RPG sub-cellular localization pattern in root hairs. (A-C) Live-cell confocal imaging of infected root hairs of WT transgenic roots co-expressing mCherry-RPG and a nuclear localized tandem CFP as transformation marker. Images were acquired at 4-5 dpi with *S. meliloti*-GFP. **(A)** Punctate structure labelled by mCherry-RPG (arrowhead) capping the IT tip ahead of *S. meliloti*-GFP colonizing the tube. **(B)** mCherry-RPG puncta localize at the tip of ITs harboring multiple branches. **(C)** Aside with a bright signal located to puncta (arrowhead), a weak signal of mCherry-RPG can be occasionally observed in the nucleus (n) of infected root hairs. **(D)** Intensity profile along the yellow transect in **(C)**. Black arrowheads indicate intensity peaks on cytoplasmic puncta. The dashed white line boxes in **(A)** and **(B)** indicate the region shown in the respective close-ups. Individual channels are shown in grey; in merged images, the GFP/CFP channel is shown in magenta and the mCherry channel is shown in green. n = nucleus. Scale bars = 10 µm.

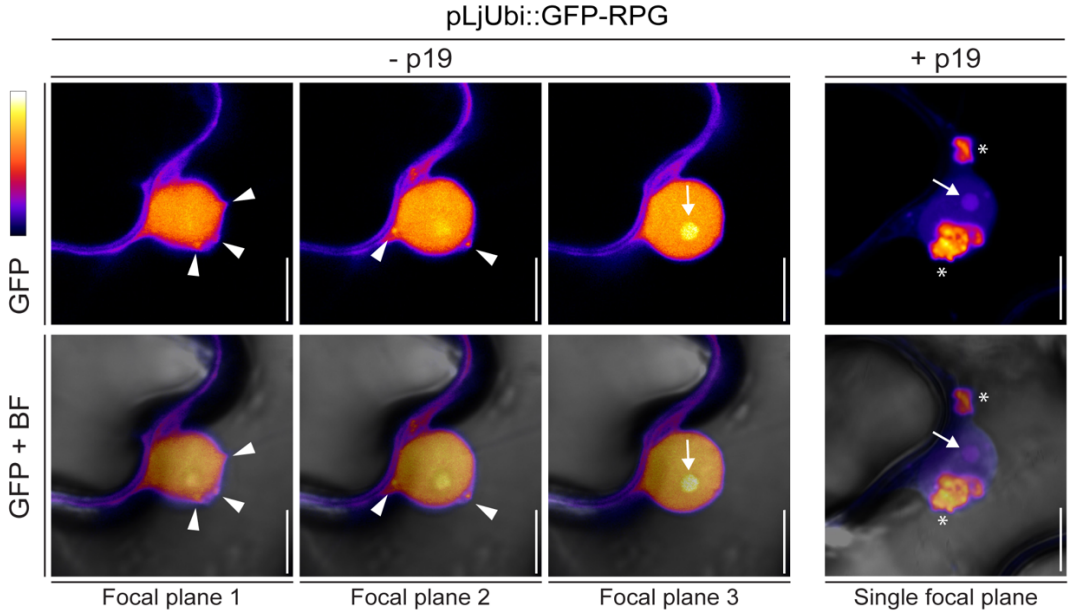

Figure 3-figure supplement 2. Subcellular localization of RPG in *N. benthamiana* epidermal cells. Live-cell confocal images of the nucleus and perinuclear region of *N. benthamiana* epidermal cells ectopically expressing GFP-RPG. In the absence of the silencing suppressor p19, GFP-RPG localizes in the nucleus, nucleolus (arrow) and in discrete puncta (arrowheads) located in the perinuclear region. Addition of p19 enhances accumulation of GFP-RPG in perinuclear associated structures (asterisks). The GFP channel is colored in Fire with yellow showing the maximum intensity and purple a low level of fluorescence. The bright field (BF) is overlaid with the GFP channel. Scale bars = 10 µm.

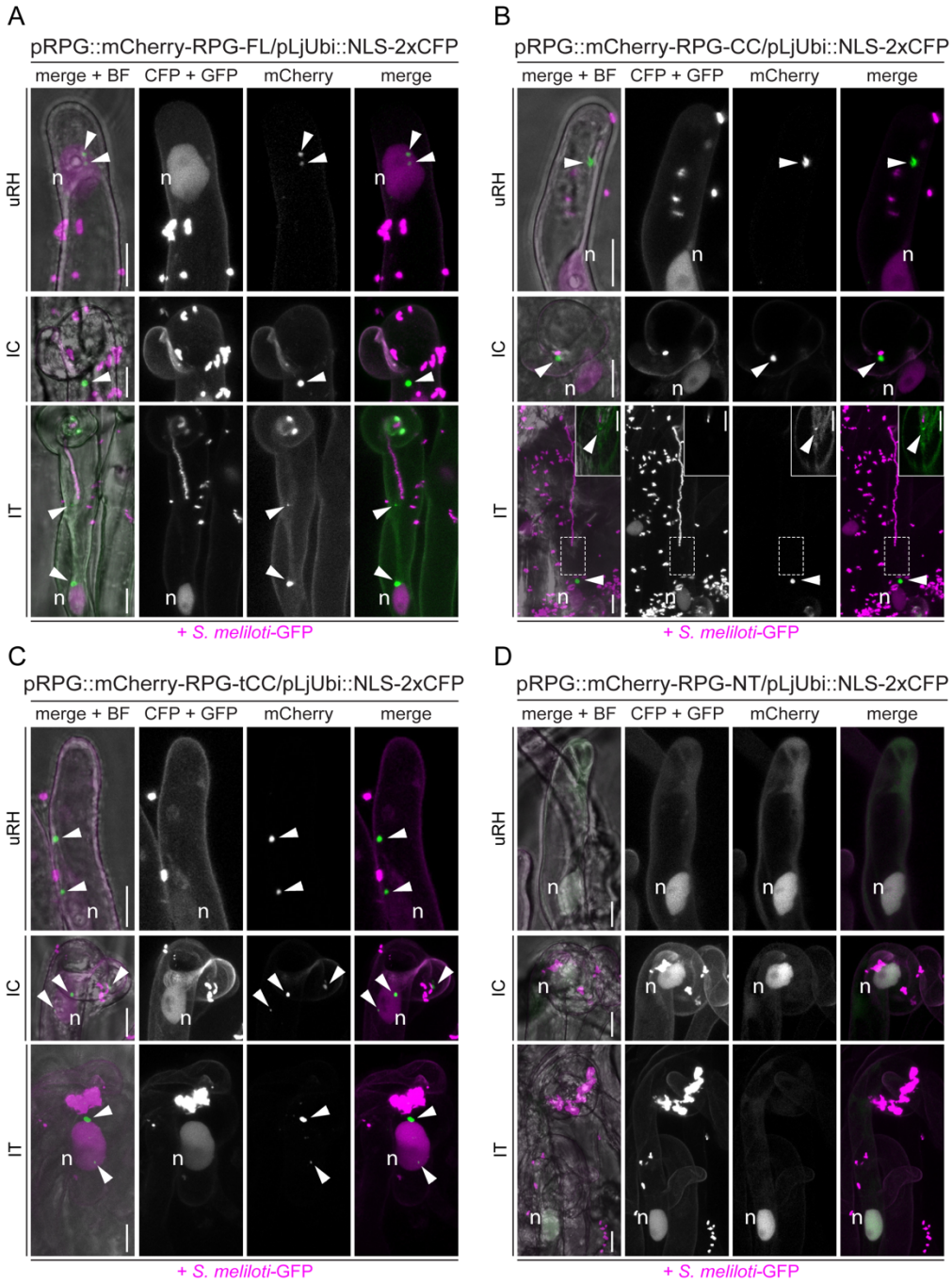

Figure 3-figure supplement 3. The coiled-coil region is necessary and sufficient to drive RPG localization to puncta. Live-cell confocal images of root hairs from *rpg-1* transgenic roots expressing mCherry-RPG and its deletion derivative imaged at 4-7 dpi with *S. meliloti*-GFP. For each construct, uninfected root hairs (uRH), curled root hairs hosting infection chambers (IC) and root hairs harboring infection threads (IT) were imaged. mCherry-FL **(A),** mCherry-RPG-CC **(B)** and mCherry-RPG-tCC **(C)** accumulate in bright punctate structures (arrowheads) in root hairs at different stages, while mCherry-NT **(D)** localizes in the nucleus and the cytoplasm. Images are intensity projections. Individual channels are shown in grey; in merged images, the GFP/CFP channel is shown in magenta and the mCherry channel is shown in green. A nuclear-localized tandem CFP was used as transformation marker. The dashed white line boxes in **(B)** indicate the region shown in the corresponding insets. Images in the insets are FLIM-based scans (20 repetitions) of single focal planes (CFP + GFP channel = 2.43 ns; mCherry channel = 1.38 ns; threshold = 10 photons). n = nucleus. Scale bars = 10 µm.

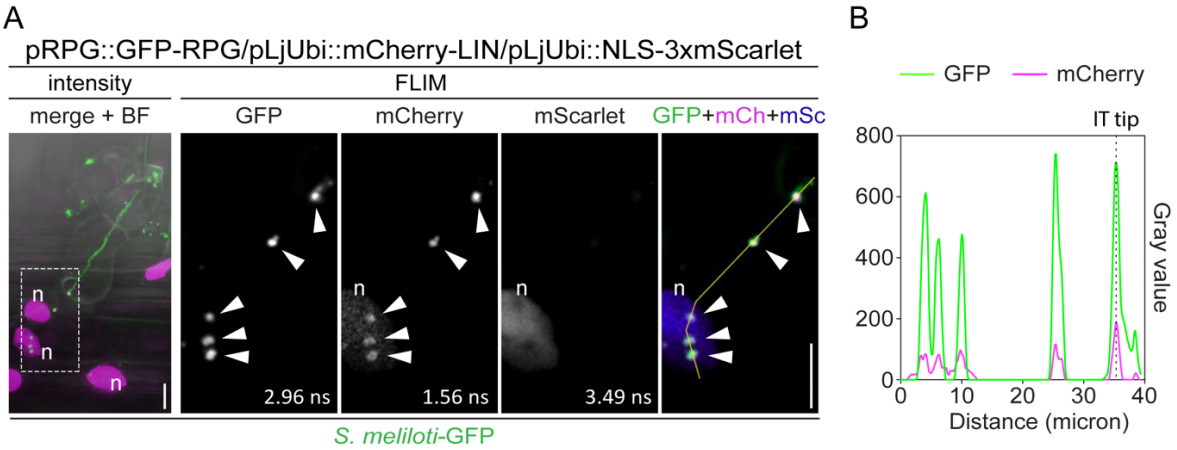

Figure 3-figure supplement 4. RPG co-localizes with LIN during root hair infection. (A) Live-cell confocal images of infected root hairs from transgenic WT roots showing co-localization of GFP-RPG with mCherry-LIN in punctate structures (arrowheads) located at the IT tip, in the perinuclear space and in the cytoplasm between these two poles. Weak signal of mCherry-LIN is visible in the nucleus (n). The intensity-based image is a merge of intensity projections of GFP (green) and mCherry/mScarlet (magenta) channels overlaid with the brightfield (BF) channel. The dashed white line box indicates the region shown in FLIM images. FLIM images are single focal planes with individual channels shown in grey. Lifetime values (ns) obtained from exponential reconvolution of decay profiles of GFP and mCherry/mScarlet channels are reported. When components are merged, GFP is shown in green, mCherry in magenta and mScarlet in blue. A nuclear-localized triple mScarlet was used as transformation marker. n = nucleus. Scale bars = 10 µm. Images are representative of 3 composite plants analyzed. **(B)** Intensity profile along the yellow transect shown in **(A)**. The intensity peaks at the infection thread tip (IT tip) are marked by a dashed black line.

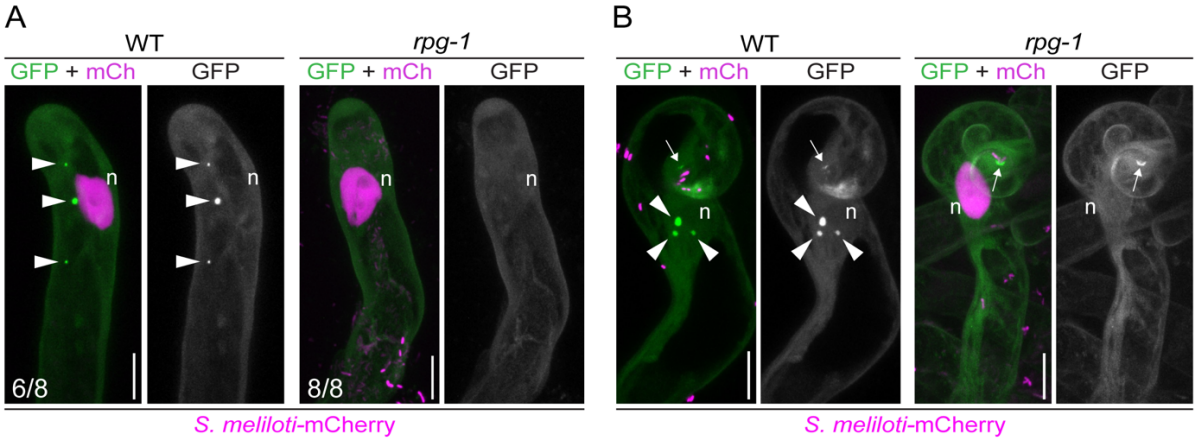

Figure 3-figure supplement 5. VPY recruitment to puncta is dependent on RPG. Live-cell confocal images of root hairs from transgenic WT and *rpg-1* roots expressing VPY-GFP. **(A)** VPY-positive cytoplasmic puncta (arrowheads) visible in WT uninfected root hairs are not maintained in *rpg-1*. **(B)** Accumulation of VPY-GFP adjacent to the site of rhizobia infection (arrows) occurs in few root hairs of *rpg-1* transgenic roots but it is not accompanied by bright punctate structures (arrowheads) associated to the nucleus (n) as seen in root hairs of WT transgenic roots. The GFP channel is shown in grey when isolated, in green when merged with mCherry (magenta). A nuclear-localized tandem mCherry was used as transformation marker. Numbers indicate frequencies of observations, made on a total number of 6 (WT) and 7 (*rpg-1*) composite plants. n = nucleus. Scale bars = 10 µm

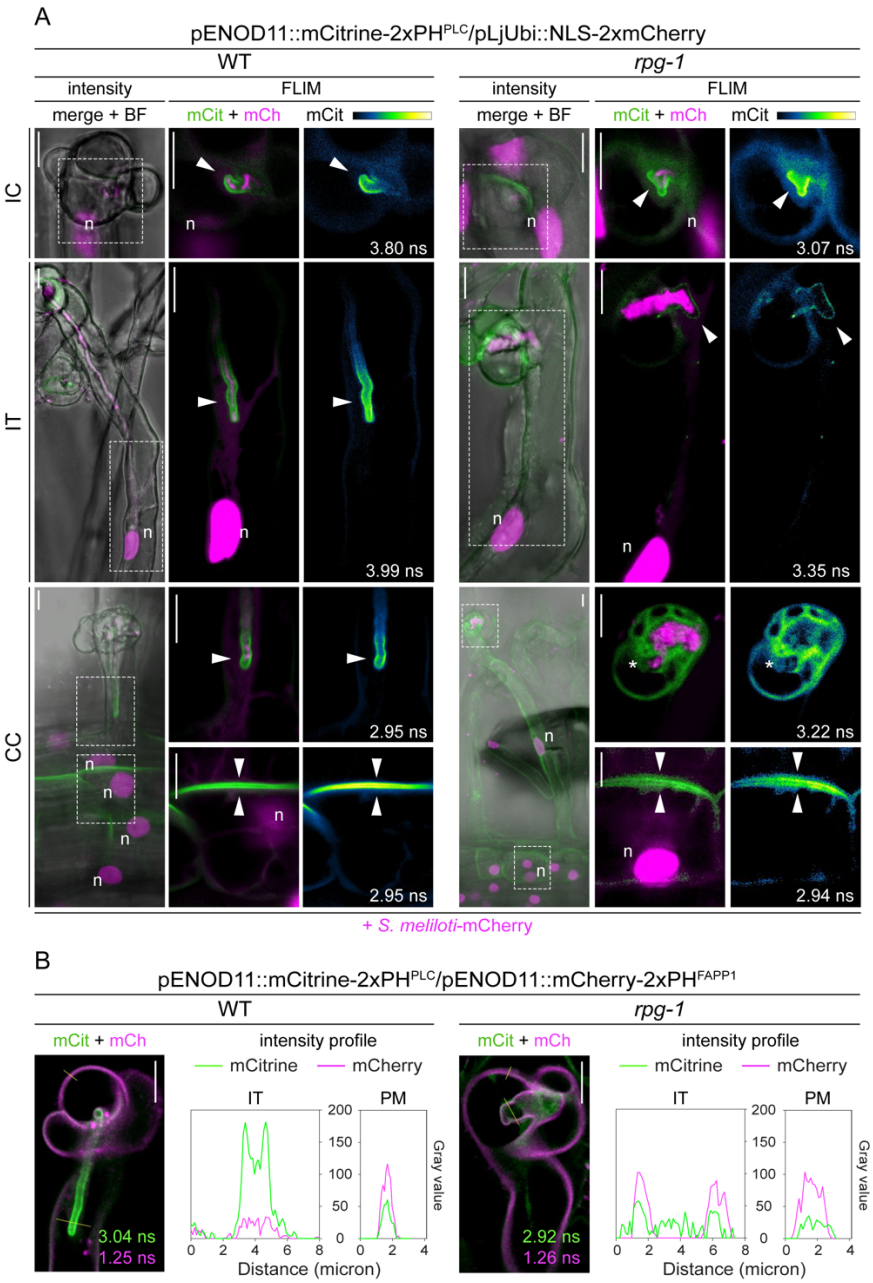

Figure 4. RPG is required to maintain strong membrane polarization at the IT tip. (A) Live-cell confocal images of root hairs from transgenic WT and *rpg-1* roots expressing the PI(4,5)P_2 biosensor mCitrine-2xPH^{PLC} at 4-8 dpi with *S. meliloti*-mCherry. The distribution of mCitrine-2xPH^{PLC} in WT and *rpg-1* transgenic roots is compared during emergence of rhizobia from the infection chamber (IC), in root hairs hosting infection threads (IT) and in cortical cells underlying epidermal infection events (CC). Membrane domains where differential enrichment of PI(4,5)P_2 occurred are indicated with arrowheads. Cytoplasmic signal of the biosensor in *rpg-1* infected root hairs is indicated with an asterisk. Intensity-based images are a merge of intensity projections of mCitrine (green) and mCherry (magenta) channels overlaid with the brightfield (BF) channel. The dashed white line box in intensity images indicates the region shown in FLIM images. FLIM images are single focal planes; the mCitrine component is shown in green when merged with the mCherry component (magenta) and in Green Fire Blue when isolated, with yellow indicating the maximum intensity and blue a low level of fluorescence. Lifetime values (ns) obtained from exponential reconvolution of decay profiles of the mCitrine channel are reported. A nuclear-localized tandem mCherry was used as transformation marker. n = nucleus. Scale bars = 10µm. **(B)** Co-visualization of PI4P and PI(4,5)P_2 in root hairs harboring ITs from WT and *rpg-1* transgenic plants co-expressing mCitrine-2xPH^{PLC} and mCherry-2xPH^{FAPP1} at 4 dpi with *S. meliloti*-LacZ. Images are merge of mCitrine (green) and mCherry (magenta) components with indicated lifetime obtained from exponential reconvolution of decay profiles of the respective channels. Intensity profiles show grey values along the yellow transects intersecting the infection thread membrane (IT) and the root hair plasma membrane (PM) in the corresponding images. Scale bars = 10 µm.

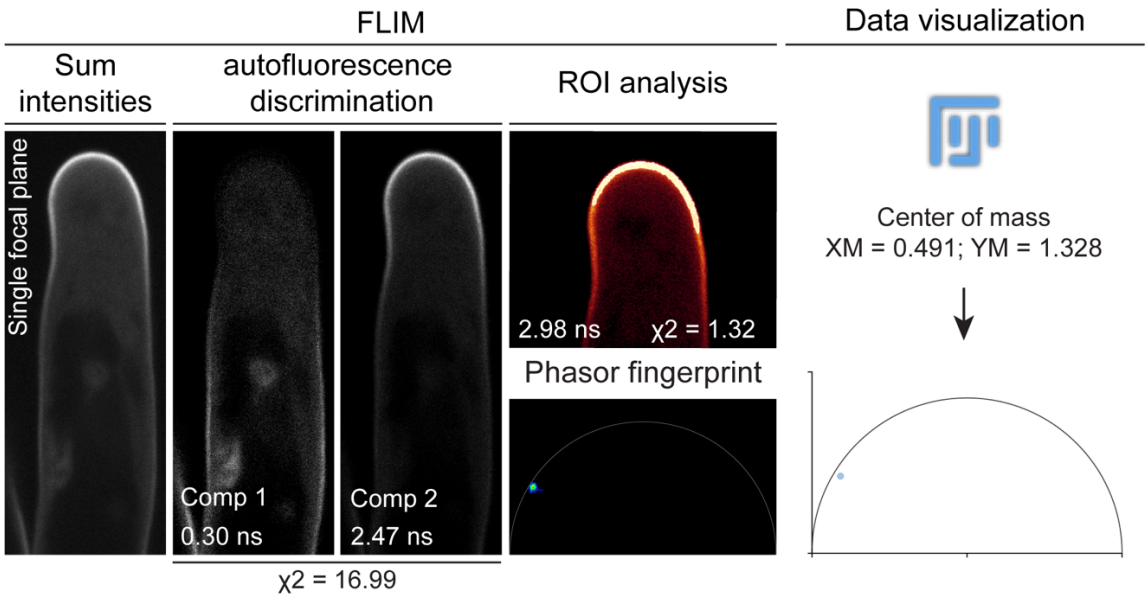

Figure 4-figure supplement 1. A FLIM-based systematic approach adopted to visualize PI(4,5)P_2 membrane enrichment. The sequential steps used for visualization and analysis of PI(4,5)P_2 distribution patterns are shown in a confocal image of a root hair from WT transgenic roots expressing mCitrine-PH^{PLC} as example. FLIM-based confocal imaging initially yields an image (sum intensities) where the intensities of the different fluorescent components present in the scanned area are summed up. By applying n-exponential reconvolution of the fluorescence intensity decay profile of the whole image, the major fluorescent components are separated and a lifetime value is assigned to each of them. The number of components is determined according to a reduced chi-squared ($\chi 2$) criterion (Lakowicz, 2006). The components exhibiting lifetime values ≤ 1.1 ns are considered as autofluorescence and are subtracted from the image. To determine with higher accuracy the enrichment of mCitrine-PH^{PLC} at the apical membrane domain, the decay profile at such region of interest (ROI) is analyzed. The lifetime is calculated via mathematical fitting, yielding a more precise estimation, as shown by the chi-squared ($\chi 2$) reaching values closer to 1. A lifetime value of ~ 3 ns for mCitrine is consistent with previous reports (Söhnel et al., 2016). In addition, Phasor fingerprints of fluorescence emissions at the ROIs are generated using the fit-free Phasor approach, which assigns a position to each pixel in the ROI according to its composition in term of fluorescent species (Malacrida et al., 2021). Enrichment of the mCitrine-PH^{PLC} biosensor at the apical membrane domain results in pixels forming a cloud positioned on or close to the semicircle in the left part of the plot, where long mono-exponential decays are located. The Phasor fingerprint is further converted to a point in an XY plot by measuring the center of mass of the pixel population in the Phasor image using ImageJ/(Fiji) (Schindelin et al., 2012). In this way, data can be visualized on a graph.

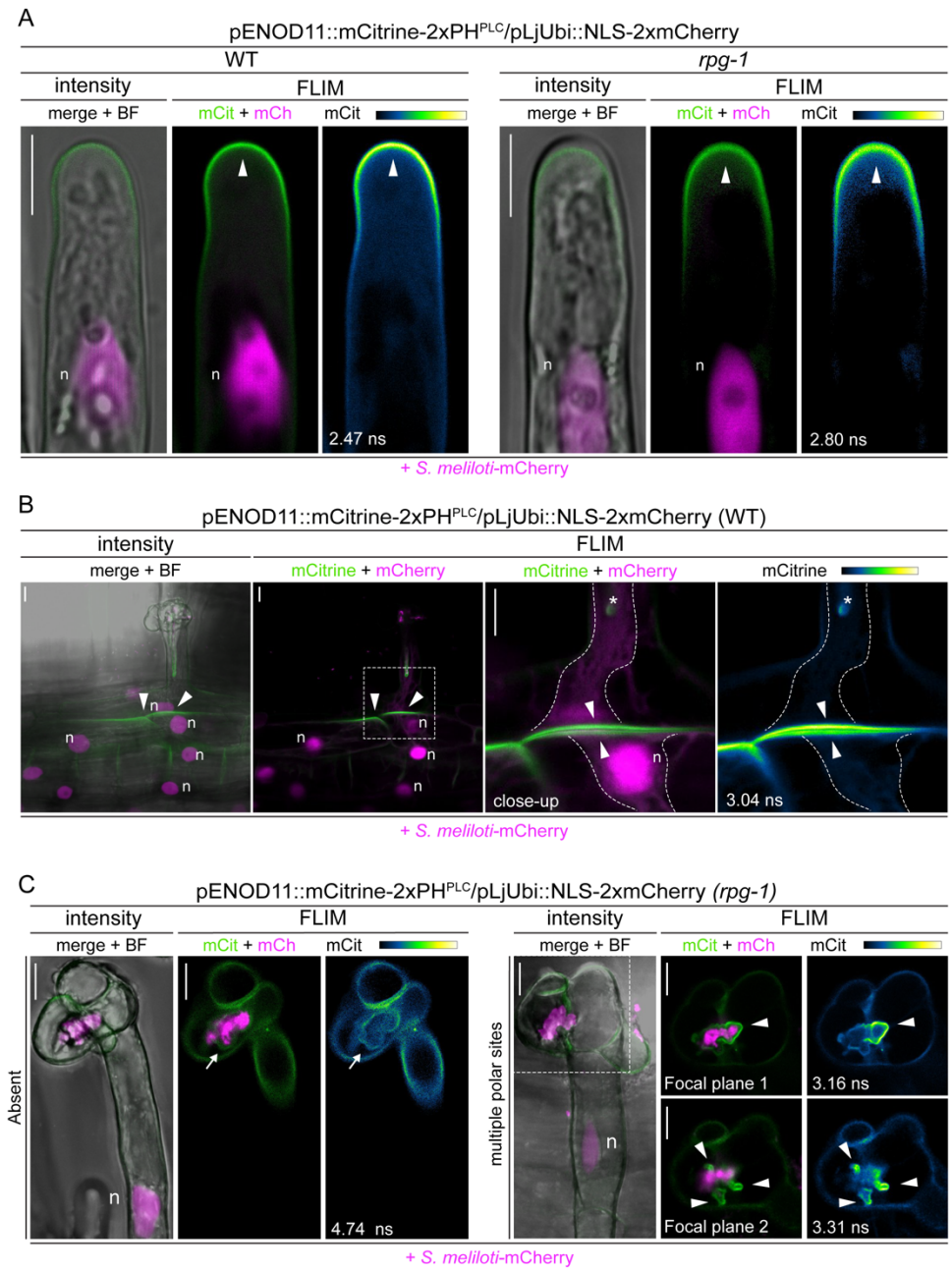

Figure 4-figure supplement 2. PI(4,5)P_2 patterning in transgenic roots of WT and *rpg-1*. Live-cell confocal images of WT and *rpg-1* transgenic roots expressing the PI(4,5)P_2 biosensor mCitrine-2xPH^{PLC} at 4-8 dpi with *S. meliloti*-mCherry. **(A)** Accumulation of PI(4,5)P_2 (arrowhead) at the apical membrane of growing root hairs occurring in both WT and *rpg-1* transgenic roots. **(B)** PI(4,5)P_2 enrichment (arrowheads) at the basal domain of infected root hairs and at the apical membrane of underlying cortical cells visualized in WT transgenic roots (enlarged panels of Figure 4A-CC). mCherry-derived cytoplasmic signals occurring due to leakage of the nuclear-localized transformation marker highlight the presence of a cytoplasmic column (dashed freehand line) connecting the tip of the IT (asterisk) to the base of the root hair and surrounding the nucleus (n) in the underlying cortical cells. The dashed white line box indicates the region shown in the close-up. **(C)** Representative images of infected root hairs on *rpg-1* transgenic roots showing an almost absent signal of the PI(4,5)P_2 biosensor on the membrane (arrow, left panel) or its presence at multiple polar sites (arrowheads, right panel) on enlarged infection structures. The dashed white line indicates the region shown in focal plane 1 and 2. Intensity-based images are a merge of intensity projections of mCitrine (green) and mCherry (magenta) channels overlaid with the brightfield (BF) channel. FLIM images are single focal planes; the mCitrine component is shown in green when merged with the mCherry component (magenta) and in Green Fire Blue when isolated, with yellow indicating the maximum intensity and blue a low level of fluorescence. Lifetime values (ns) obtained from exponential reconvolution of decay profiles of the mCitrine channel are reported. n = nucleus. Scale bars = 10 µm.

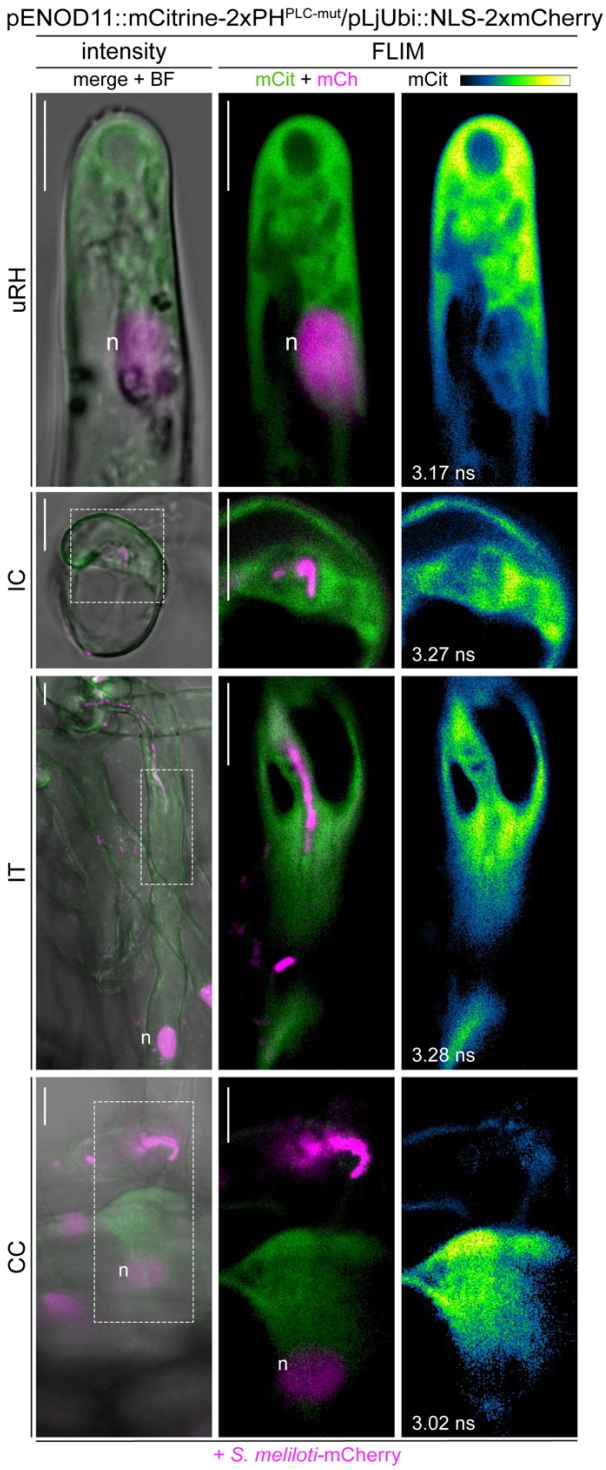

Figure 4-figure supplement 3. A mutant PI(4,5)P_2 biosensor does not accumulate at membrane domains during rhizobial infection. Live-cell confocal images of WT transgenic roots expressing the mCitrine-2xPH$^{PLC\ mut}$ biosensor at 4-7 dpi with *S. meliloti*-mCherry. The signal from the mutated version of the biosensor appeared diffused in the cytoplasm of uninfected (uRH) and infected (IC-IT) root hairs, and in cortical cells (CC) on the infection thread trajectory. Intensity-based images are a merge of mCitrine (green) and mCherry (magenta) channels overlaid with the brightfield (BF) channel. FLIM images are single focal planes; the mCitrine component is shown in green when merged with the mCherry component (magenta) and in Green Fire Blue when isolated, with yellow indicating the maximum intensity and blue a low level of fluorescence. Lifetime values (ns) obtained from exponential reconvolution of decay profiles of the mCitrine channel are reported. Images are representative of 3 composite plants analyzed. n = nucleus. Scale bars = 10 µm.

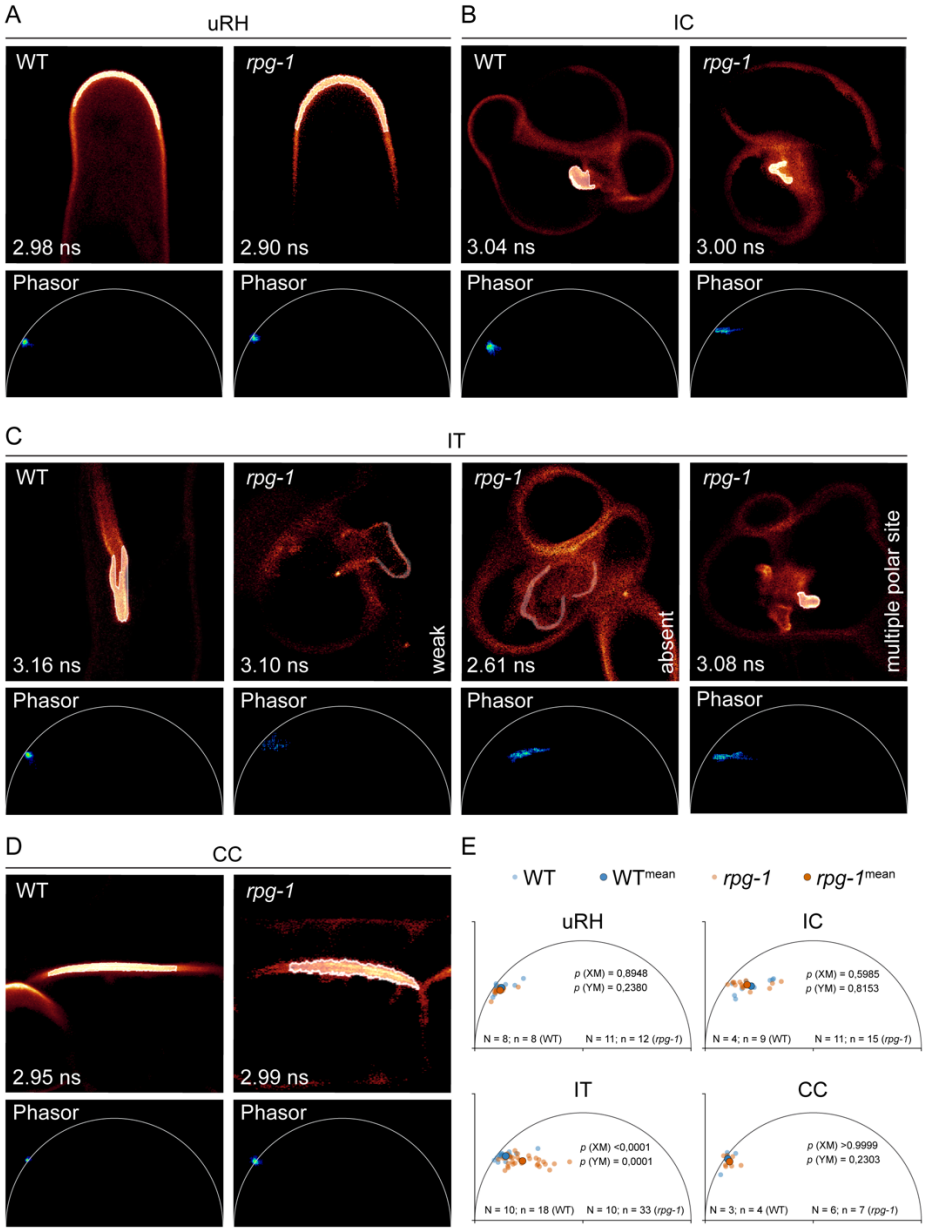

Figure 4-figure supplement 4. Phasor analysis statistically supports loss of IT membrane polarization occurring in *rpg-1*. Estimation of PI(4,5)P_2 membrane enrichment in WT and *rpg-1* transgenic roots expressing the PI(4,5)P_2 biosensor mCitrine-PH^{PLC} via analysis of fluorescence emission at regions of interest (ROI) corresponding to different membrane domains. **(A-D)** Representative FLIM images of analyzed membrane domains showing the Phasor fingerprint (Phasor) associated to the ROI selected on the membrane (white outlines) and the lifetime value (ns) calculated via fitting of the decay profile of the ROI. Phasor fingerprints of ROIs selected at the apex of uninfected root hairs (uRH) **(A)**, at the site of symbiont emergence from the infection chamber (IC) **(B)** and on the membrane domain on the trajectory of IT propagation in cortical cells (CC) **(D)** in cells of WT and *rpg-1* transgenic root show similar positioning on the left half of the Phasor plot close to the semicircle, indicative of similar PI(4,5)P_2 enrichment. **(C)** The Phasor signature associated to the membrane of ITs in *rpg-1* markedly differs from the signature of WT ITs: a pixel cloud with similar Phasor position but composed of few scattered pixels is indicative of weak signal of the mCitrine-PH^{PLC} biosensor, while a consistent shift of the pixel cloud away from the semicircle towards the right part of the plot where short lifetimes are located is indicative of dominance of autofluorescent components over mCitrine-PH^{PLC}, whose signal appears mostly absent. The Phasor fingerprint associated to the membrane surrounding the multiple polar sites emerging from the enlarged infection threads in *rpg-1* is similar to the one recorded at the IC of *rpg-1* in **(B)**. **(E)** XY plots representing the center of mass calculated from Phasor fingerprints of different membrane domains analyzed in multiple cells of different plants for each genotype. A Mann-Whitney test was applied to detect statistical differences between XM and YM values. Calculated *p* values are shown. N = number of plants; n = number of cells.

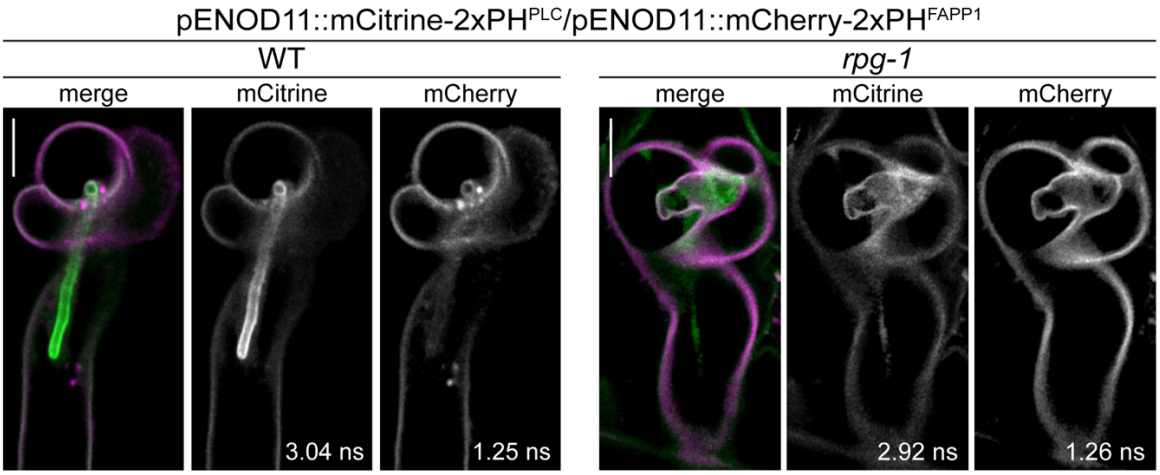

Figure 4-figure supplement 5. Co-visualization of PI4P and PI(4,5)P_2 in WT and *rpg-1* infected root hairs. FLIM-based confocal images of infected root hairs shown in Figure 4B from WT and *rpg-1* transgenic plants co-expressing mCitrine-2xPH^{PLC} and mCherry-2xPH^{FAPP1} at 4 dpi with *S. meliloti*-LacZ. Images are single focal planes with individual channels shown in grey. Lifetime values (ns) obtained from exponential reconvolution of decay profiles of mCitrine and mCherry channels are reported. When components are merged, mCitrine is shown in green and mCherry in magenta. Scale bars = 10 µm.

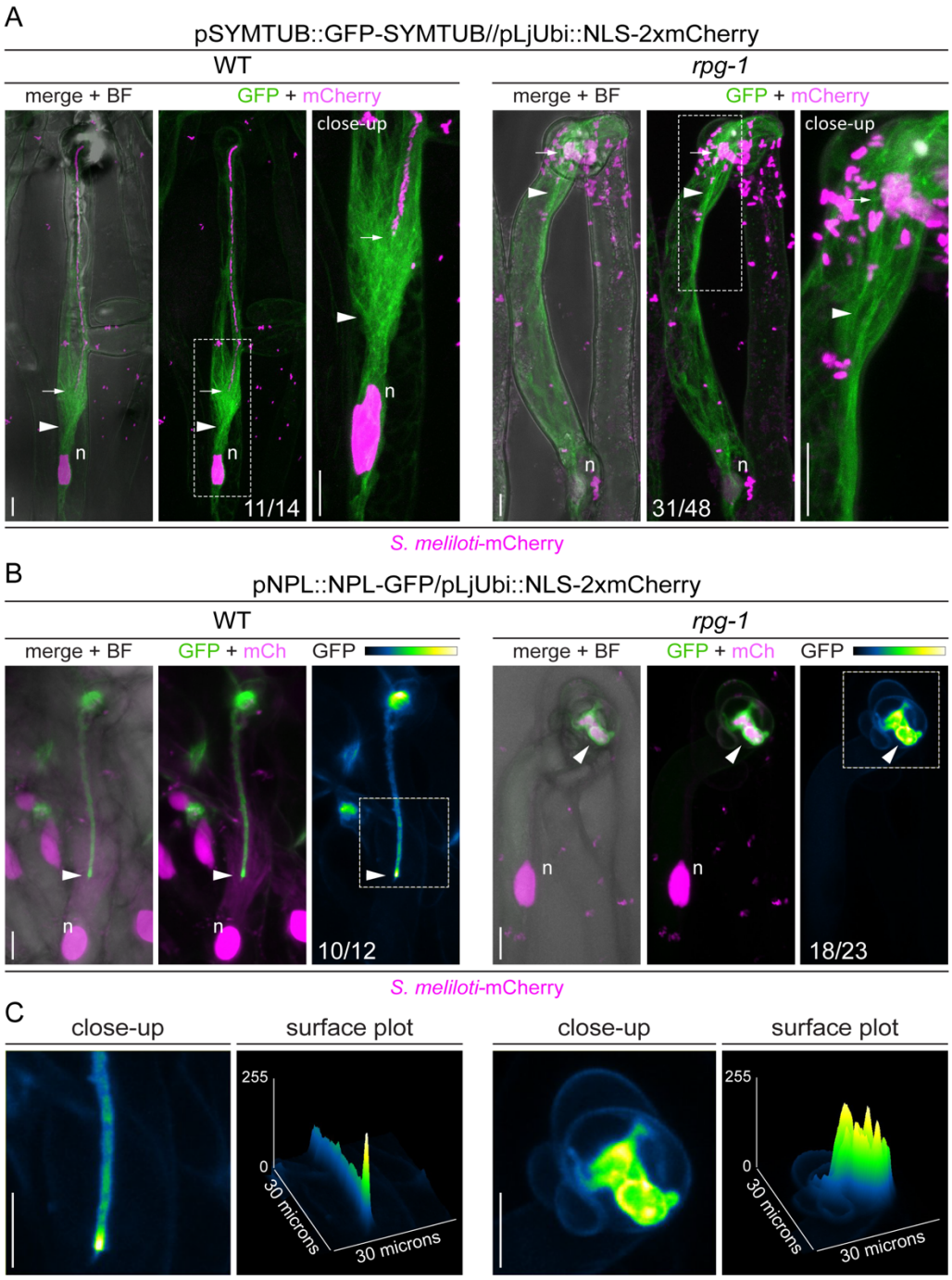

Figure 5. The tip-to-nucleus microtubule connectivity and polar secretion of NPL are affected in *rpg-1*. (A) In vivo imaging of microtubule patterning in root hairs hosting infection threads from WT and *rpg-1* transgenic roots expressing GFP-SYMTUB at 4-8 dpi with *S. meliloti*-mCherry. The endoplasmic microtubule array (arrowhead) bridging the nucleus (n) and the IT tip (arrow) in WT root hairs appears stretched in *rpg-1* root hairs, where the IT tip exhibit a tilted direction of growth. Images are merge of intensity projections of GFP (green) and mCherry (magenta) channels. The brightfield (BF) channel is overlaid with the merge. The dashed white line boxes indicate the region shown in the close-up. Numbers indicate frequencies of observation made on a total number of 6 (WT) and 14 (*rpg-1*) composite plants. **(B)** Live-cell confocal images showing focal accumulations of NPL-GFP at the IT tip (arrowhead) in WT root hairs in contrast to its unrestricted distribution in the apoplastic space surrounding ITs developed within root hairs of *rpg-1* transgenic roots. Images are intensity projections. The GFP channel is shown in green when merged with the mCherry channel (magenta), or in Green Fire Blue when isolated, with yellow indicating the maximum intensity and blue a low level of fluorescence. The brightfield (BF) channel is overlaid with the merge. Numbers indicate frequencies of observations made on a total number of 6 plants (WT and *rpg-1*). **(C)** Close-up and surface plot of the regions bounded by the dashed white line boxes in **(B).** The signal of NPL-GFP in WT ITs is described by a single peak compared to multiple peaks detected in *rpg-1*. Scale bars = 10 µm.

Source Data Files

Figure 1 – source data 1
IT diameter and statistical analysis

Figure 1 – figure supplement 1 – source data 1
Nodule number and statistical analysis

Figure 2 – source data
IT diameter and statistical analysis

Figure 3 - source data 1
FLIM fit values and intensity profile values

Figure 3 - source data 2
Raw images of Western Blot analysis

Figure 3 – figure supplement 1 – source data 1
Intensity profile values

Figure 3 – figure supplement 4 – source data 1
FLIM fit values and intensity profile values

Figure 4 - source data 1
FLIM fit values and intensity profile values

Figure 4 – figure supplement 1 – source data 1
FLIM fit values

Figure 4 – figure supplement 2 – source data 1
FLIM fit values

Figure 4 – figure supplement 3 – source data 1
FLIM fit values

Figure 4 – figure supplement 4 – source data 1
FLIM fit values and Phasor analysis values